

Building the largest spectroscopic sample of ultra-compact massive galaxies with the Kilo Degree Survey

DIANA SCOGNAMIGLIO,^{1,2} CRESCENZO TORTORA,³ MARILENA SPAVONE,¹ CHIARA SPINIELLO,^{1,4} NICOLA R. NAPOLITANO,^{5,1}
GIUSEPPE D'AGO,⁶ FRANCESCO LA BARBERA,¹ FEDOR GETMAN,¹ NIVYA ROY,⁵ MARIA ANGELA RAJ,¹ MARIO RADOVICH,⁷
MASSIMO BRESCIA,¹ STEFANO CAVUOTI,^{1,8} LÉON V.E. KOOPMANS,⁹ KONRAD H. KUIJKEN,¹⁰ GIUSEPPE LONGO,⁸ AND
CARLO E. PETRILLO⁹

¹*INAF – Osservatorio Astronomico di Capodimonte, Salita Moiariello 16, 80131 - Napoli, Italy*

²*Argelander-Institut für Astronomie, Auf dem Hügel 71, D-53121 - Bonn, Germany*

³*INAF - Osservatorio Astronomico di Arcetri, L.go E. Fermi 5, 50125 - Firenze, Italy*

⁴*European Southern Observatory, Karl-Schwarzschild-Str. 2, 85748 - Garching, Germany*

⁵*School of Physics and Astronomy, Sun Yat-sen University Zhuhai Campus, Daxue Road 2, 519082 -
Tangjia, Zhuhai, Guangdong, P.R. China*

⁶*Instituto de Astrofísica Pontificia Universidad Católica de Chile, Avenida Vicuña Mackenna, 4860 - Santiago, Chile*

⁷*INAF – Osservatorio Astronomico di Padova, Vicolo Osservatorio 5, 35122 - Padova, Italy*

⁸*Dipartimento di Scienze Fisiche, Università di Napoli Federico II, Compl. Univ. Monte S. Angelo, 80126 - Napoli, Italy*

⁹*Kapteyn Astronomical Institute, University of Groningen, P.O. Box 800, 9700 AV - Groningen, the Netherlands*

¹⁰*Leiden Observatory, Leiden University, P.O. Box 9513, 2300 RA - Leiden, the Netherlands*

Submitted to ApJ

ABSTRACT

Ultra-compact massive galaxies UCMGs, i.e. galaxies with stellar masses $M_{\star} > 8 \times 10^{10} M_{\odot}$ and effective radii $R_e < 1.5$ kpc, are very rare systems, in particular at low and intermediate redshifts. Their origin as well as their number density across cosmic time are still under scrutiny, especially because of the paucity of spectroscopically confirmed samples. We have started a systematic census of UCMG candidates within the ESO Kilo Degree Survey, together with a large spectroscopic follow-up campaign to build the largest possible sample of confirmed UCMGs. This is the third paper of the series and the second based on the spectroscopic follow-up program. Here, we present photometrical and structural parameters of 33 new candidates at redshifts $0.15 \lesssim z \lesssim 0.5$ and confirm 19 of them as UCMGs, based on their nominal spectroscopically inferred M_{\star} and R_e . This corresponds to a success rate of $\sim 58\%$, nicely consistent with our previous findings. The addition of these 19 newly confirmed objects, allows us to fully assess the systematics on the system selection, and finally reduce the number density uncertainties. Moreover, putting together the results from our current and past observational campaigns and some literature data, we build the largest sample of UCMGs ever collected, comprising 92 spectroscopically confirmed objects at $0.1 \lesssim z \lesssim 0.5$.

This number raises to 116, allowing for a 3σ tolerance on the M_{\star} and R_e thresholds for the UCMG definition. For all these galaxies we have estimated the velocity dispersion values at the effective radii which have been used to derive a preliminary mass–velocity dispersion correlation.

Keywords: galaxies: evolution - galaxies: general - galaxies: elliptical and lenticular, cD - galaxies: structure

1. INTRODUCTION

The discovery that massive, quiescent galaxies at redshift $z > 2$ are extremely compact with respect to their local counterparts (Daddi et al. 2005; Trujillo et al. 2006; van Dokkum et al. 2010; Damjanov et al. 2009, 2011) has opened a new line of investigation within the context of galaxy formation and evolution. In particular, the strong galaxy size growth (Daddi et al. 2005; Trujillo

et al. 2006) needed to account for the difference in compactness from high- to low- z , finds the best explanation in the so-called two-phase formation model (Oser et al. 2010). First of all, massive and very compact gas-rich disk objects are created due to dissipative inflows of gas. These so-called “blue nuggets” form stars “in situ” at high rate, and this causes a gradual stellar and halo mass growth (Dekel & Burkert 2014). Subsequently, the star formation in the central region quenches and the blue nuggets quickly (and passively) evolve into compact “red nuggets”.

In many cases, the masses of these high- z red nuggets are similar to those of local giant elliptical galaxies, which indicates that almost all the mass is assembled during this first formation phase. However, their sizes are only about a fifth of the size of local ellipticals of similar mass (Werner et al. 2018). Thus, during the second phase of this scenario, at lower redshifts, red nuggets undergo dry mergers with lower mass galaxies growing in size (but only slightly increasing their masses) and becoming, over billions of years, present-day ETGs.

Nevertheless, given the stochastic nature of mergers, a small fraction of the red nuggets slips through the cosmic time untouched and without accreting any stars from satellites and mergers: the so-called “relics” (Ferré-Mateu et al. 2017). These galaxies have assembled early on in time and have somehow missed completely the size growth. They are therefore supposedly made of only “in situ” stellar population and as such they provide a unique opportunity to track the formation of this specific galaxy stellar component, which is mixed with the accreted one in normal massive ETGs.

Indeed, very massive, extremely compact systems have been already found at intermediate to low redshifts, also including the local Universe (Trujillo et al. 2009, 2014; Taylor et al. 2010; Valentinuzzi et al. 2010; Shih & Stockton 2011; Läsker et al. 2013; Poggianti et al. 2013a,c; Hsu et al. 2014; Stockton et al. 2014; Damjanov et al. 2015a,b; Ferré-Mateu et al. 2015; Saulder et al. 2015; Stringer et al. 2015; Yıldırım et al. 2015; Wellons et al. 2016; Gargiulo et al. 2016a; Tortora et al. 2016, 2018b; Charbonnier et al. 2017; Beasley et al. 2018; Buitrago et al. 2018). Ultra-Compact Massive Galaxies (UCMGs hereafter), defined here as objects with stellar mass $M_* > 8 \times 10^{10} M_\odot$ and effective radius $R_e < 1.5$ kpc (although sometimes other stellar mass and effective radius ranges are adopted, see Section 2) are the best relics candidates.

The precise abundance of relics, and even more generally of UCMGs, without any age restriction, at low redshifts is an open issue. In fact, at $z \leq 0.5$, a strong disagreement exists between simulations and observa-

tions and among observations themselves on the number density of UCMGs and its redshift evolution. From a theoretical point of view, simulations predict that the fraction of objects that survive without undergoing any significant transformation since $z \sim 2$ is about $1 - 10\%$ (Hopkins et al. 2009; Quilis & Trujillo 2013), and at the lowest redshifts (i.e., $z \lesssim 0.2$), they predict densities of relics of $10^{-7} - 10^{-5} \text{ Mpc}^{-3}$. This is in agreement with the lower limit given by NGC 1277, the first discovered local ($z \sim 0.02$) compact galaxy with old stellar population, which is the first prototype of local “relic” of high- z nuggets (Trujillo et al. 2014), and the most updated estimate of $6 \times 10^{-7} \text{ Mpc}^{-3}$ set by Ferré-Mateu et al. (2017), who report the discovery of two new confirmed, local “relics”. In the near-by Universe, large sky surveys as the Sloan Digital Sky Survey (SDSS¹) show a sharp decline in compact galaxy number density of more than three orders of magnitude below the high-redshift values (Trujillo et al. 2009; Taylor et al. 2010). In contrast, Poggianti et al. (2013a,c) suggest that the abundance of low-redshift compact systems might be even comparable with the number density at high redshift. Moreover, data from the WINGS survey of near-by clusters (Fasano et al. 2006; Valentinuzzi et al. 2010) estimate, at $z \sim 0$, a number density of two orders of magnitude above the estimates based on the SDSS dataset.

Since the situation in the local Universe is very complex and different studies report contrasting results, it is crucial to increase the UCMG number statistics in the range $0.1 \lesssim z \lesssim 0.5$, where these systems should be more common. In recent years different works have contributed to the census of UCMGs in wide-field surveys at these redshifts (Tortora et al. 2016, 2018b; Charbonnier et al. 2017; Buitrago et al. 2018). In particular, within the Kilo Degree Survey (KiDS, see Section 2) collaboration, we have undertaken a systematic search for UCMGs in the intermediate redshift range with the aim of building a large spectroscopically-confirmed sample. In the first paper of the series (Tortora et al. 2016, hereafter T16), we collected a sample of $\lesssim 100$ candidates in the first $\sim 156 \text{ deg}^2$ of KiDS (corresponding to an effective area of $\sim 107 \text{ deg}^2$, after masking). In the second paper (Tortora et al. 2018b, hereafter T18) we updated the analysis and extended the study to the third KiDS Data Release (KiDS-DR3). We have collected a sample of ~ 1000 candidates, building the largest sample of UCMG candidates at $z < 0.5$, assembled to date over the largest sky area (333 deg^2).

¹ <https://www.sdss.org/>

It is worth noticing that most of all the previously published findings on these peculiar objects are based on photometric samples. However, after identification of the candidates, spectroscopic validation is necessary to obtain precise spectroscopic redshifts and confirm the compactness of the systems. Thus, in T18 we presented the first of such spectroscopic validation, with data obtained at Telescopio Nazionale Galileo (TNG) and at the New Technology Telescope (NTT).

In this third paper of the series we therefore continue the work started in T18 to spectroscopically validate UCMGS and derive their “true”² number densities at intermediate redshifts. In particular, we present here spectroscopic observations for 33 new KiDS UCMG candidates and add to these all the spectroscopic confirmed UCMGS publicly available in the literature to update the UCMG number density distribution, already presented in T18, at redshift $0.15 < z < 0.5$. Finally, we also obtain and present here the velocity dispersion measurements (σ) for the new 33 UCMGS and for the 28 UCMGS from T18. Finally, we present a preliminary correlation between stellar mass and velocity dispersion of these rare objects, with the aim of starting to fully characterize the properties of these systems.

This paper represents a further step forward to our final goal, which is to unequivocally prove that a fraction of the red and dead nuggets, which formed at $z > 2$, evolved undisturbed and passively into local “relics”. In particular, to be classified as such, the objects have to 1) be spectroscopically validated UCMGS, 2) have a very old stellar populations (e.g., assuming a formation redshift $z_{\text{phot}} \gtrsim 2$, the stellar population age needs to be $t \gtrsim 10$ Gyrs). Since we do not derive stellar ages, this paper makes significant progress only on the first part of the full story, as not all the confirmed UCMGS satisfy a stringent criterion on its stellar age. We are confident that most of our confirmed UCMGS will likely be old, as we showed in T18 that most of the candidates presented very red optical and near-infrared colours. Moreover, in the spectra we present here (see Section 3), we find spectral features typical of passive stellar population. However, only with higher resolution and high signal-to-noise spectra, which would allow us to perform an in-depth stellar population analysis, it will be possible to really disentangle relics from younger UCMGS. The detailed stellar population analysis is also particularly important as a fraction of our UCMGS also shows some hint of recent star formation or of younger stellar population. This has been already seen in other samples too (Tru-

jillo et al. 2009; Ferré-Mateu et al. 2012; Poggianti et al. 2013a; Damjanov et al. 2015a,b; Buitrago et al. 2018), but it is not necessarily in contrast with the predictions from galaxy assembly simulations (see e.g. Wellons et al. 2015). In fact, they find that ultra-compact systems host accretion events, but still keep their bulk of stellar population old and the compact structure almost unaltered. Hence, higher quality spectroscopical data will be mandatory to perform a multi-population analysis and possibly confirm also this scenario.

The layout of the paper is as follows. In Section 2, we briefly describe the KiDS sample of high signal-to-noise ratio (S/N) galaxies, the subsample of our photometrically selected UCMGS, the objects we followed-up spectroscopically, and the impact of the selection criteria we use. In Section 3 we give an overview on observations and data reduction, and we discuss the spectroscopic redshift and velocity dispersion calculation procedures. In Section 4, we discuss the main results, i.e. the number density as a function of redshift and the the impact of systematics on these number densities. We also derive a tentative relation between the stellar mass and the velocity dispersion at the effective radius of our sample of UCMGS, compared with a sample of normal-sized elliptical galaxies at similar masses and redshifts. Finally, in Section 5, we summarize our findings and discuss future perspectives. In the Appendix we report the final validated UCMGS catalog where some redshifts come from our spectroscopic program and others from the literature. For all galaxies we give structural parameters in the g , r , i , bands and the u , g , r , i , aperture photometry from KiDS.

Throughout the paper, we assume $H_0 = 70 \text{ km s}^{-1} \text{ Mpc}^{-1}$, $\Omega_m = 0.3$, and $\Omega_\Lambda = 0.7$ (Komatsu et al. 2011).

2. SAMPLE DEFINITION

KiDS is one of the ESO public wide-area surveys (1350 deg² in total) being carried out with the VLT Survey Telescope (VST; Capaccioli & Schipani 2011). It provides imaging data with unique image quality (pixel scale of 0.21/pixel and a median r -band seeing of 0.65”) and baseline ($ugri$ in optical + $ZYJHK$ if combined to VIKING (Edge et al. 2014; Wright et al. 2018)). These features make the data very suitable for measuring structural parameters of galaxies, including very compact systems, up to $z \sim 0.5$ (Roy et al. 2018; T16; T18). Both image quality and baseline are very important for the selection of UCMGS as they allow us to mitigate systematics that might have plagued previous analyses from the ground.

As baseline sample of our search, we use the data included in the third Data Release of KiDS (KiDS-DR3)

² With the word “true”, we mean here the number density obtained with a spectroscopically confirmed sample.

presented in de Jong et al. (2017), consisting of 440 survey tiles ($\approx 333 \text{ deg}^2$, after masking). The galaxy data sample is described in the next Section 2.1.

2.1. Galaxy data sample

From the KiDS multi-band source catalog (de Jong et al. 2015, 2017), we built a catalog of ~ 5 million galaxies (La Barbera et al. 2008) within KiDS-DR3, using SExtractor (Bertin & Arnouts 1996). Since we mainly follow the same selection procedure of T16 and T18, we refer the interested reader to these papers for more general details. Here we only list relevant physical quantities for the galaxies in the catalog, explaining how we obtain them and highlighting the novelty of the set-up we use in the stellar mass calculation:

- *Integrated optical photometry.* We use aperture magnitudes `MAGAP_6`, measured within circular apertures of $6''$ diameter, Kron-like `MAG_AUTO` as the total magnitude and Gaussian Aperture and PSF (GAaP) magnitudes, `MAG_GAaP` (de Jong et al. 2017) in each of the four optical bands (*ugri*).
- *Structural parameters.* Surface photometry is performed using the 2DPHOT environment (La Barbera et al. 2008), which fits galaxy images with a 2D Sérsic model. The model also includes a constant background and assumes elliptical isophotes. In order to take the galaxies best-fitted and remove those systems with a clear sign of spiral arms, we put a threshold on the goodness of the fit, only selecting $\chi^2 < 1.5$. We also calculate a modified version, χ'^2 , which includes only the central image pixels, that are generally more often affected by these substructures. 2DPHOT model fitting provides the following parameters: average surface brightness μ_e , major-axis effective radius $\Theta_{e,\text{maj}}$, Sérsic index n , total magnitude m_S , axial ratio q , and position angle. In this analysis, we use the circularized effective radius Θ_e , defined as $\Theta_e = \Theta_{e,\text{maj}} \sqrt{q}$. Effective radius is then converted to the physical scale value R_e using the measured (photometric and/or spectroscopic) redshift. Only galaxies with r -band $(S/N)_r \equiv 1/\text{MAGERR_AUTO_r} > 50$, where `MAGERR_AUTO_r` is the error on the r -band `MAG_AUTO`, are kept for the next analysis (La Barbera et al. 2008, 2010; Roy et al. 2018, T16; T18).
- *Photometric redshifts.* Redshifts are determined with the Multi Layer Perceptron with Quasi Newton Algorithm (MLPQNA) method (Brescia et al. 2013, 2014; Cavuoti et al. 2015a), and presented in Cavuoti et al. (2015b, 2017), which we refer to for all details.

- *Spectroscopic redshifts.* We cross-match our KiDS catalog with overlapping spectroscopic surveys to obtain spectroscopic redshifts for the objects in common, i.e. the `KiDS_SPEC` sample. We use redshifts from the Sloan Digital Sky Survey Data Release 9 (SDSS-DR9; Ahn et al. 2012, 2014), Galaxy And Mass Assembly Data Release 2 (GAMA-DR2; Driver et al. 2011) and 2dFLenS (Blake et al. 2016).

- *Stellar masses.* We run LE PHARE (Arnouts et al. 1999; Ilbert et al. 2006) to estimate stellar masses. This software performs a simple χ^2 fitting between the stellar population synthesis (SPS) theoretical models and the data. In order to minimize the degeneracy between colours and stellar population parameters, we fix the redshift, either using the z_{phot} or z_{spec} , depending on the availability and the sample under exam. It is evident that, when a z_{spec} is obtained for a UCMG candidate, the stellar mass needs to be re-estimated as the “true” redshift might produce a different mass that needs to be checked against the criteria to confirm the UCMG nature (see next section). Since the UCMG candidates sample analyzed in this paper has been collected using a slightly different spectral library with respect to the sample presented in T18, we use a partially different set-up to estimate stellar masses. As in T18, we fit multi-wavelength photometry of the galaxies in the sample with Single burst models from Bruzual & Charlot 2003 (BC03 hereafter). However, here we further constrain the parameter space, forcing metallicities and ages to vary in the range $0.2 \leq Z/Z_\odot \leq 2.5$ and $3 \leq t \leq t_{\text{max}}$ Gyr, respectively. The maximum age, t_{max} , is set by the age of the Universe at the redshift of the galaxy, with a maximum value of 13 Gyr at $z = 0$. The age cutoff of 3 Gyr is meant to minimize the probability of underestimating the stellar mass by obtaining a too young age, following Maraston et al. (2013). Then, as in T18, we adopt a Chabrier (2001) IMF and the observed *ugri* magnitudes `MAGAP_6` (and related 1σ uncertainties δu , δg , δr , and δi), which are corrected for Galactic extinction using the map in Schlafly & Finkbeiner (2011). In order to correct the M_* outcomes of LE PHARE for missing flux, we use the total magnitudes derived from the Sérsic fitting and the formula:

$$\log_{10} M_* = \log_{10} M_*^{\text{LE PHARE}} + 0.4 \times (\text{MAGAP_6} - m_S) \quad (1)$$

where $\log_{10} M_{\star}^{\text{LE PHARE}}$ is the output of LE PHARE. We consider calibration errors on the photometric zero-point $\delta_{z_p} \equiv (\delta u_{z_p}, \delta g_{z_p}, \delta r_{z_p}, \delta i_{z_p}) = (0.075, 0.074, 0.029, 0.055)$, quadratically added to the SExtractor magnitude errors (see T18).

- *Galaxy classification.* Using LE PHARE, we also fit the observed magnitudes with the set of 66 empirical spectral templates used in Ilbert et al. (2006), in order to determine a qualitative galaxy classification. The set is based on different templates resembling spectra of ‘‘Elliptical’’, ‘‘Spiral’’ and ‘‘Starburst’’ galaxies.

We use the above dataset, that we name KiDS_FULL, to collect a complete set of photometrically selected UCMGs, using criteria as described in the next section.

Moreover, in order to check what galaxies had already literature spectroscopy, we cross-match the KiDS_FULL with publicly available spectroscopic samples and define the so-called KiDS_SPEC sample, which comprises all galaxies from our complete photometric sample with known spectroscopic redshifts.

2.2. UCMGs selection and our sample

To select the UCMG candidates, we use the same criteria reported in T16 and T18:

1. *Massiveness:* A Chabrier-IMF based stellar mass of $M_{\star} > 8 \times 10^{10} M_{\odot}$ (Trujillo et al. 2009; T16, T18);
2. *Compactness:* A circularized effective radius $R_e < 1.5$ kpc (T18);
3. *Best-fit structural parameters:* A reduced $\chi^2 < 1.5$ in g -, r - and i - filters (La Barbera et al. 2010), and further criteria to control the quality of the fit, as $\Theta_e > 0.05''$, $q > 0.1$ and $n > 0.5$;
4. *Star/Galaxy separation:* A discrimination between stars and galaxies using the $g-J$ vs. $J-K_s$ plane to minimize the overlap of sources with the typical stellar locus (see e.g., Fig. 1 in T16).

Further details about the above criteria, to select UCMGs from both KiDS_FULL and KiDS_SPEC can be found in T16 and T18. In the following we refer to the *photometrically selected* and the *spectroscopically selected* samples as the ones where M_{\star} and R_e are calculated using z_{phot} or z_{spec} , respectively.³

After applying all the requirements we end up with the following samples at $z < 0.5$:

- UCMG_FULL: a photometrically selected sample of 1221 UCMG candidates⁴ (1256 before the colour-colour cut) extracted from KiDS_FULL;
- UCMG_SPEC: a spectroscopically selected sample of 55 UCMGs, selected from the KiDS_SPEC sample, for which stellar masses and radii have been computed using the spectroscopic redshifts;
- UCMG_PHOT_SPEC: a sample of 50 photometrically selected UCMG candidates which have spectroscopic redshift available from literature. Practically, these galaxies have been extracted from KiDS_SPEC but they resulted to be UCMG on the basis of their z_{phot} .

In the UCMG_FULL sample, that provides the most statistically significant characterization of our UCMG candidates, the objects are brighter than $r \sim 21$. Most of them are located at $z_{\text{phot}} > 0.3$, with a median redshift of $z_{\text{phot}} = 0.41$. Median values of 20.4 and 11 dex are found for the extinction corrected r -band MAG_AUTO and $\log_{10}(M_{\star}/M_{\odot})$. More than 97 per cent of the UCMG_FULL candidates have KiDS photometry consistent with ‘‘Elliptical’’ templates in Ilbert et al. (2006), and they have very red colours in the optical-NIR colour-colour plane. The $R_e < 1.5$ kpc constraint corresponds to $\Theta_e \lesssim 0.4$ arcsec, the medians for these parameters are $R_e = 1.22$ kpc and $\Theta_e = 0.23$ arcsec, respectively. The range of the values for axis ratio and Sérsic index is wide, but their distributions are peaked around values of $q \sim 0.4$ and $n \sim 4$, with median values of 0.47 and 4.6, respectively.

2.3. The impact of selection criteria

Following the previous papers of this series (T16 and T18), we adopt rather stringent criteria on the sizes and masses to select only the most extreme (and rare) UCMGs. However, there is a large variety of definitions used in other literature studies. Until there will be no consensus, the comparison among different analyses will be prone to a ‘‘definition bias’’. Here in this section we evaluate the impact of different definitions on our UCMG_FULL sample (see also a detailed discussion in

obviously scales with the true redshift) and the stellar mass (see Section 2.1) to check that the criteria of compactness and massiveness hold.

⁴ In T18 we collected 995 photometrically selected candidates (1000 before the colour-colour cut), which is different from the number of 1221 found here. The difference between these numbers is related to the different sets of masses adopted in T18 and in the present paper. We will discuss the impact of the mass assumption later in the paper, showing the effect on the number density evolution.

³ When the spectroscopic redshift becomes available for a given UCMG candidate, one has to recompute both the R_e in kpc (which

T18). For instance, keeping the threshold on the stellar mass unchanged and releasing the constraint on the size, such as $R_e < 2$ kpc and < 3 kpc, the number of candidates (before colour-colour cut) would increase to 3430 and 12472, respectively. Instead, decreasing the threshold in mass from $\log_{10}(M_*/M_\odot) = 10.9$ to 10.7, the number of selected galaxies within UCMG_FULL would not change by more than 3%, i.e. the size criterion is the one impacting more the UCMG definition. Besides the threshold in size and mass, another important assumption that might significantly impact our selection is the shape of the stellar Initial Mass Function (IMF). Here, we assume a universal Chabrier IMF for all the galaxies despite recent claims for a bottom-heavier IMF in more massive ETGs (e.g. Conroy et al. 2012; Cappellari et al. 2012; Spiniello et al. 2012; Tortora et al. 2013; La Barbera et al. 2013, Spiniello et al. 2014, 2015). This choice has been made to compare our results with other results published in the literature, all assuming a Chabrier IMF. If a Salpeter IMF were to be used instead, more coherently with predictions for compact and massive systems (Martín-Navarro et al. 2015; Ferré-Mateu et al. 2017), keeping the massiveness and compactness criteria unchanged, we would retrieve 1291 UCMGs instead of 1256. Thus, also the IMF slope has a negligible impact on our selection.

3. SPECTROSCOPIC OBSERVATIONS

Having obtained a large sample of UCMG candidates, the natural next step is their spectroscopical confirmation. In other terms, a spectroscopic confirmation of their photometric redshifts is crucial to confirm them as UCMGs since both compactness and massiveness are originally based on the z_{phot} associated to the photometric sample. In this work we present the spectroscopic follow-up of 33 objects. Twenty-nine candidates are extracted from UCMG_FULL, while the remaining 4 come from the data sample assembled in T16⁵. The basic photometric properties of these 33 objects are reported in Table 1. The structural parameters and the r -band 2D fit outputs derived from 2DPHOT are reported in Table 2 and the fits themselves are showed in Figure 1⁶.

⁵ The sample in T16 was assembled in the early 2015, applying the same criteria listed in Section 2.2. It consisted of a mixture of the 149 survey tiles from KiDS-DR1/2 (de Jong et al. 2015) and few other tiles that have been part of subsequent releases. Although this datasample and the KiDS_FULL one are partially overlapping in terms of sky coverage, they differ in the photometry, structural parameter values and photometric redshifts.

⁶ The r -band KIDS images sometimes seem to suggest some stripping or interactions with other systems. However the majority of the spectra are typical of a passive, old stellar population. Moreover, we also note that according to the simulations presented

Data have been collected in the years 2017 and 2018 during three separate runs, two carried out with the 3.6m Telescopio Nazionale Galileo (TNG), and one using the 2.54m Isaac Newton Telescope (INT), both located at Roque de los Muchachos Observatory (Canary Islands). We thus divide our sample into three sub-groups, according to the observing run they belong to: UCMG_INT_2017, UCMG_TNG_2017 and UCMG_TNG_2018. They consist of 13, 11 and 9 UCMG candidates, respectively, with $\text{MAG_AUTO_r} \lesssim 20.5$ and $z_{\text{phot}} \lesssim 0.45$.

In the following sections, we discuss the instrumental and observational set-up as well as the data reduction steps for the two different instrumentation. Then we describe the S/N determination and the redshift and velocity dispersion calculation, obtained with the new Optimised Modelling of Early-type Galaxy Aperture Kinematics pipeline (OMEGA-K, D’Ago et al., in prep).

3.1. INT spectroscopy

Data on 13 luminous UCMG candidates belonging to the UCMG_INT_2017 sample have been obtained with the IDS spectrograph during 6 nights at the INT telescope, in visitor mode (PI: C. Tortora, ID: 17AN005). The observations have been carried on with the RED+2 detector and the low resolution grating R400V, covering the wavelength range from 4000 to 8000 Å. The spectra have been acquired with long-slits of 1.6'' or 2'' width, providing a spectral resolution of $\Delta\lambda/\lambda = 560$, a dispersion of 1.55 Å/pixel, and a pixel scale of 0.33 arcsec/pixel. The average seeing during the observing run was FWHM $\sim 1.5''$, the single exposure time ranged between 600 and 1200 seconds and from 1 up to 5 single exposures have been obtained per target, depending on their magnitudes.

Data reduction has been performed using IRAF⁷ image processing packages. The main data reduction steps include dark subtraction, flat-fielding correction and sky subtraction. The wavelength calibration has been performed by means of comparison spectra of CuAr+CuNe lamps acquired for each observing night using the IDENTIFY task. A sky spectrum has been extracted from the outer edges of the slit, and subtracted from each row of the two dimensional spectra using the IRAF task BACKGROUND in the TWODSPEC.LONGSLIT package. The sky-

in Wellons et al. (2016), compact galaxies can undertake a variety of evolutionary paths, including some interaction with a close-by companion, without changing their compactness.

⁷ IRAF is distributed by the National Optical Astronomy Observatories, which is operated by the Associated Universities for Research in Astronomy, Inc. under cooperative agreement with the National Science Foundation.

Table 1. Integrated photometry for the 33 UCMG candidates observed within our spectroscopic program, 13 in UCMG_INT_2017, 11 in UCMG_TNG_2017 and 9 in UCMG_TNG_2018 (within each subsample the galaxies are ordered by Right Ascension). From left we give: a) progressive ID number; b) KIDS identification name; c) r -band KiDS `MAG_AUTO`; d-g) u -, g -, r - and i -band KiDS magnitudes measured in an aperture of 6 arcsec of diameter with 1σ errors; h) photometric redshift from machine learning. All the magnitudes have been corrected for galactic extinction using the maps of [Schlafly & Finkbeiner \(2011\)](#). More details are provided in Section 2.

ID	name	MAG_AUTO_r	u_6''	g_6''	r_6''	i_6''	z_{phot}
Observation date: March 2017		Instrument: INT/IDS					
1	KIDS J085700.29-010844.55	19.21	22.70 ± 0.21	20.74 ± 0.01	19.22 ± 0.003	18.71 ± 0.01	0.28
2	KIDS J111108.43+003207.00	19.05	22.49 ± 0.14	20.46 ± 0.01	19.04 ± 0.003	18.61 ± 0.006	0.26
3	KIDS J111447.86+003903.71	19.00	22.35 ± 0.12	20.47 ± 0.01	19.03 ± 0.003	18.57 ± 0.009	0.26
4	KIDS J111504.01+005101.16	19.21	20.43 ± 0.02	19.92 ± 0.006	19.24 ± 0.003	19.01 ± 0.014	0.45
5	KIDS J111750.31+003647.35	19.13	22.80 ± 0.19	20.74 ± 0.01	19.12 ± 0.003	18.69 ± 0.01	0.37
6	KIDS J122009.53-024141.88	18.69	21.93 ± 0.1	20.02 ± 0.007	18.71 ± 0.002	18.19 ± 0.006	0.22
7	KIDS J122639.96-011138.08	18.59	22.15 ± 0.11	20.06 ± 0.008	18.63 ± 0.003	18.21 ± 0.008	0.23
8	KIDS J122815.38-015356.06	18.84	22.17 ± 0.1	20.26 ± 0.008	18.84 ± 0.003	18.37 ± 0.008	0.24
9	KIDS J140127.77+020509.13	19.04	21.47 ± 0.06	20.23 ± 0.007	19.01 ± 0.003	18.65 ± 0.007	0.34
10	KIDS J141120.06+023342.62	18.85	22.72 ± 0.17	20.47 ± 0.01	18.83 ± 0.003	18.39 ± 0.007	0.32
11	KIDS J145700.42+024502.06	18.62	22.17 ± 0.13	19.95 ± 0.008	18.67 ± 0.002	18.23 ± 0.007	0.24
12	KIDS J150309.55+001318.10	18.99	22.59 ± 0.19	20.47 ± 0.01	19.02 ± 0.003	18.67 ± 0.007	0.28
13	KIDS J152844.81-000912.86	18.56	22.91 ± 0.25	19.98 ± 0.01	18.59 ± 0.002	18.20 ± 0.005	0.23
Observation date: March 2017		Instrument: TNG/DOLORES					
14	KIDS J084239.97+005923.71	19.63	22.95 ± 1.76	21.14 ± 0.12	19.58 ± 0.04	19.02 ± 0.08	0.35
15	KIDS J090412.45-001819.75	19.11	22.51 ± 0.95	20.58 ± 0.07	19.13 ± 0.02	18.66 ± 0.02	0.27
16	KIDS J091704.84-012319.65	19.21	22.87 ± 1.03	20.84 ± 0.08	19.20 ± 0.02	18.65 ± 0.02	0.33
17	KIDS J104051.66+005626.73	19.52	23.27 ± 0.29	20.97 ± 0.02	19.54 ± 0.005	18.52 ± 0.01	0.33
18	KIDS J114800.92+023753.02	19.41	23.13 ± 0.33	20.54 ± 0.01	19.41 ± 0.005	18.61 ± 0.009	0.32
19	KIDS J120203.17+025105.56	19.43	22.57 ± 0.18	20.95 ± 0.02	19.41 ± 0.005	18.95 ± 0.01	0.30
20	KIDS J121856.54+023241.69	19.23	22.75 ± 0.17	20.79 ± 0.01	19.23 ± 0.004	18.70 ± 0.008	0.30
21	KIDS J140257.62+011730.39	19.96	23.31 ± 0.48	21.33 ± 0.02	19.94 ± 0.008	19.44 ± 0.02	0.33
22	KIDS J145656.68+002007.41	19.46	22.99 ± 0.23	20.84 ± 0.02	19.43 ± 0.005	18.94 ± 0.006	0.28
23	KIDS J145948.65-024036.57	18.57	21.96 ± 0.88	19.92 ± 0.05	18.58 ± 0.02	18.10 ± 0.04	0.25
24	KIDS J152700.54-002359.09	19.64	24.54 ± 1.45	21.19 ± 0.03	19.62 ± 0.006	19.12 ± 0.01	0.33
Observation date: March 2018		Instrument: TNG/DOLORES					
25	KIDS J083807.31+005256.58	19.29	22.48 ± 0.14	20.66 ± 0.01	19.29 ± 0.004	18.75 ± 0.009	0.28
26	KIDS J084412.25-005850.00	19.67	22.76 ± 0.22	21.16 ± 0.02	19.64 ± 0.006	19.10 ± 0.015	0.32
27	KIDS J084413.29+014847.59	19.78	23.01 ± 0.32	21.22 ± 0.02	19.75 ± 0.008	19.21 ± 0.014	0.33
28	KIDS J090933.87+014532.21	19.55	23.13 ± 0.35	21.14 ± 0.02	19.51 ± 0.005	18.98 ± 0.01	0.33
29	KIDS J092030.99+012635.38	19.52	22.70 ± 0.19	20.96 ± 0.02	19.51 ± 0.005	19.04 ± 0.015	0.29
30	KIDS J092407.03-000350.69	19.87	24.06 ± 0.55	21.48 ± 0.02	19.84 ± 0.005	19.20 ± 0.012	0.39
31	KIDS J103951.25+002402.34	19.63	22.41 ± 0.15	20.66 ± 0.01	19.62 ± 0.006	18.70 ± 0.013	0.41
32	KIDS J145721.54-014009.02	19.43	23.12 ± 0.35	21.03 ± 0.02	19.47 ± 0.004	18.97 ± 0.014	0.29
33	KIDS J152706.54-001223.64	19.67	23.92 ± 0.73	21.39 ± 0.03	19.68 ± 0.006	19.08 ± 0.01	0.43

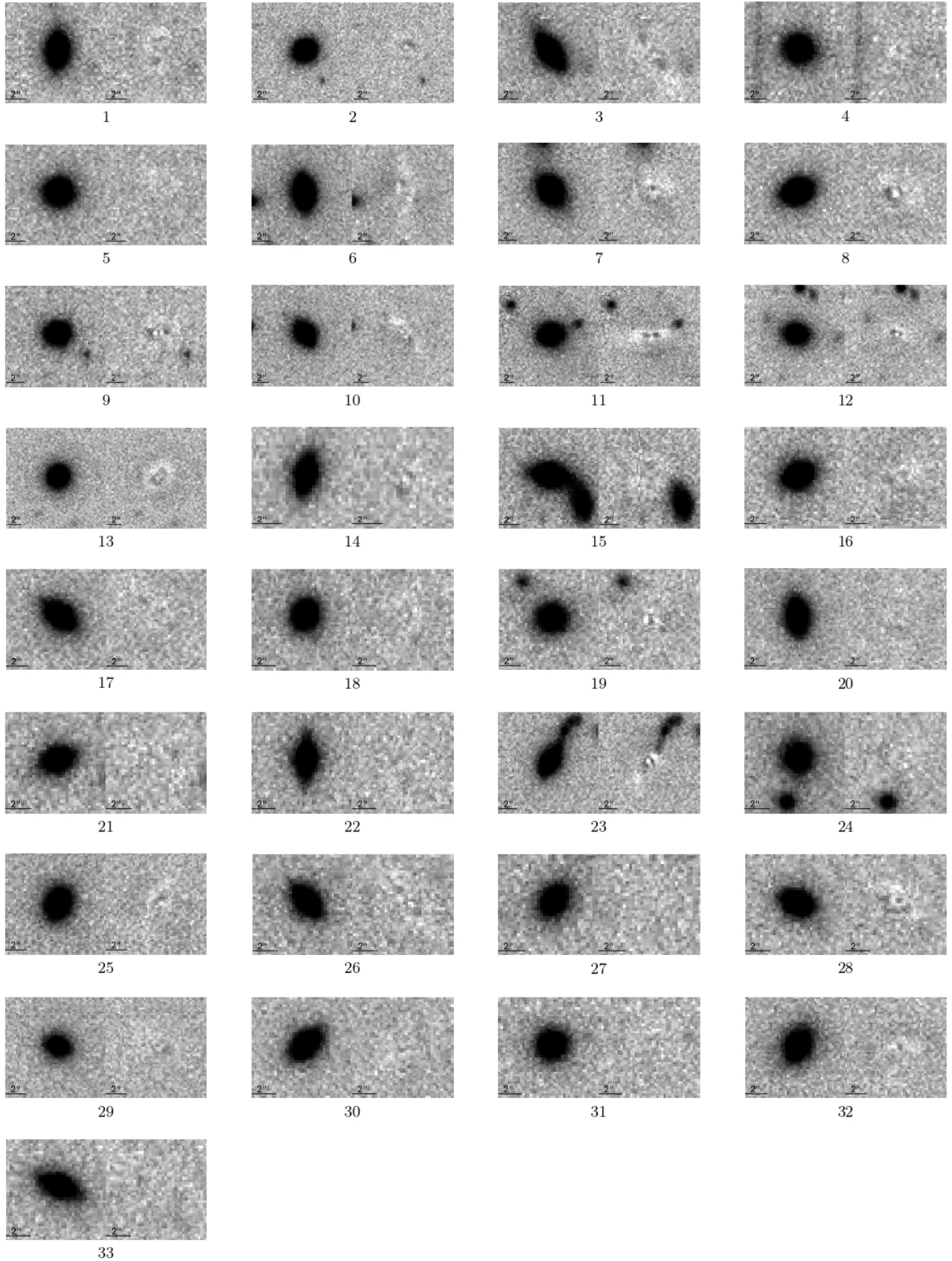


Figure 1. 2D fit output from the 2DPHOT procedure on the 33 UCMG candidates for which we obtained new spectroscopic data. For each UCMG the left panel shows the original r -band image and the right panel shows the residual after the subtraction of the 2D single Sérsic PSF convolved model. We also indicate the scale of 2 arcsec in the panels.

Table 2. Structural parameters derived running 2DPHOT on g -, r - and i -bands. For each band we give: a) circularized effective radius Θ_e , measured in arcsec, b) circularized effective radius R_e , measured in kpc (calculated using z_{phot} values listed in Table 1), c) Sérsic index n , d) axis ratio q , e) χ^2 of the surface photometry fit, f) χ'^2 of the surface photometry fit including only central pixels and g) the signal-to-noise ratio S/N of the photometric images, defined as the inverse of the error on `MAG_AUTO`.

ID	g -band							r -band							i -band						
	Θ_e	R_e	n	q	χ^2	χ'^2	S/N	Θ_e	R_e	n	q	χ^2	χ'^2	S/N	Θ_e	R_e	n	q	χ^2	χ'^2	S/N
1	0.32	1.36	2.94	0.31	1.01	0.92	81	0.37	1.55	2.33	0.33	1.02	0.98	81	0.34	1.43	4.04	0.33	1.01	1.01	98
2	0.40	1.60	3.31	0.74	1.02	0.96	100	0.28	1.11	5.54	0.76	1.02	1.07	100	0.31	1.23	5.83	0.77	1.02	1.02	161
3	0.36	1.45	4.56	0.25	0.99	1.02	94	0.26	1.06	6.08	0.26	1.03	1.20	94	0.34	1.36	4.93	0.24	1.00	1.00	108
4	0.06	0.32	2.96	0.71	1.00	1.02	148	0.06	0.35	6.32	0.87	1.03	1.12	148	0.10	0.55	5.57	0.73	0.97	0.97	62
5	0.16	0.84	7.10	0.81	1.01	0.99	90	0.14	0.71	6.83	0.87	1.07	1.08	90	0.14	0.70	6.00	0.73	1.00	1.00	108
6	0.43	1.52	1.52	0.29	1.02	0.94	134	0.35	1.23	2.15	0.26	1.02	1.16	134	0.41	1.44	2.11	0.31	0.99	0.99	148
7	0.22	0.82	8.46	0.57	1.02	1.07	118	0.31	1.12	7.53	0.68	1.03	1.28	118	0.36	1.32	2.87	0.61	1.00	1.00	123
8	0.39	1.48	2.96	0.53	1.03	0.98	125	0.36	1.36	2.68	0.54	1.03	1.19	125	0.35	1.34	2.87	0.56	1.05	1.05	128
9	0.20	0.97	4.95	0.79	1.04	1.02	161	0.24	1.14	5.19	0.83	1.04	1.20	161	0.22	1.04	5.30	0.72	0.99	0.99	166
10	0.40	1.10	2.49	0.30	1.00	1.01	97	0.21	0.97	2.97	0.30	1.15	1.20	97	0.21	0.98	2.83	0.31	0.99	1.02	156
11	0.39	1.47	7.86	0.51	1.00	0.91	104	0.27	1.02	6.71	0.42	1.04	1.23	377	0.34	1.31	8.40	0.49	0.99	0.99	129
12	0.32	1.37	6.08	0.48	1.00	1.03	79	0.31	1.30	7.16	0.56	1.07	1.14	283	0.30	1.27	6.93	0.52	1.02	0.93	132
13	0.28	1.61	3.94	0.36	1.00	1.07	135	0.39	1.45	4.24	0.77	1.04	1.19	421	0.41	1.50	5.33	0.77	1.01	0.88	175
14	0.28	1.37	2.22	0.12	1.03	0.94	53	0.23	1.12	3.27	0.29	1.00	1.07	158	0.28	1.40	3.38	0.41	0.98	0.91	105
15	0.43	1.77	4.82	0.32	1.00	1.20	70	0.27	1.13	2.69	0.36	1.04	1.15	297	0.21	0.87	4.37	0.33	1.00	0.99	244
16	0.28	1.35	3.05	0.32	1.02	1.08	70	0.24	1.14	3.03	0.41	1.04	1.18	252	0.27	1.28	4.12	0.41	1.02	1.03	219
17	0.36	1.71	4.57	0.36	1.00	0.93	58	0.31	1.46	6.10	0.38	1.02	1.01	58	0.31	1.47	4.35	0.36	0.99	0.99	91
18	0.27	1.25	2.09	0.58	1.00	0.95	93	0.29	1.36	2.83	0.58	1.03	1.04	93	0.26	1.22	2.75	0.56	1.05	1.05	114
19	0.31	1.38	6.47	0.99	1.04	1.01	59	0.29	1.29	9.54	0.89	1.03	1.09	59	0.36	1.58	5.24	0.87	1.01	1.01	111
20	0.31	1.37	2.05	0.19	1.03	0.93	82	0.33	1.46	2.75	0.30	1.02	1.00	82	0.26	1.15	3.13	0.26	1.03	1.03	132
21	0.17	0.81	6.43	0.44	1.01	0.96	52	0.11	0.50	8.05	0.46	1.03	1.12	52	0.19	0.90	4.08	0.58	1.03	1.03	70
22	0.25	1.04	2.48	0.10	1.04	1.12	74	0.12	0.50	5.60	0.20	1.03	1.11	74	0.11	0.45	5.53	0.31	1.03	1.03	184
23	0.27	1.07	6.15	0.30	1.04	1.39	110	0.31	1.22	4.34	0.30	1.04	2.78	110	0.66	2.57	8.19	0.04	1.00	1.02	146
24	0.39	1.85	10.02	0.94	1.01	1.07	42	0.14	0.67	8.83	0.75	1.01	1.16	42	0.22	1.07	9.16	0.68	1.02	1.02	73
25	0.31	1.30	4.08	0.41	0.99	0.92	84	0.35	1.49	4.02	0.45	1.03	1.06	84	0.30	1.27	3.08	0.40	1.03	0.87	106
26	0.27	1.28	2.00	0.32	1.01	1.01	58	0.29	1.36	2.69	0.36	1.04	1.15	58	0.27	1.26	4.37	0.33	1.02	0.99	75
27	0.32	1.51	6.83	0.44	1.00	0.98	51	0.23	1.11	4.36	0.52	0.98	0.90	51	0.26	1.26	6.56	0.49	1.01	0.94	78
28	0.26	1.24	1.74	0.36	1.03	1.04	55	0.24	1.14	2.66	0.48	1.08	1.28	55	0.22	1.03	3.08	0.43	1.01	0.99	109
29	0.35	1.50	5.72	0.65	1.02	1.04	51	0.33	1.42	6.92	0.68	1.01	0.96	51	0.27	1.17	8.25	0.73	1.01	0.94	70
30	0.18	0.95	6.19	0.25	1.00	0.99	50	0.26	1.39	2.82	0.32	1.00	1.05	50	0.26	1.35	2.66	0.34	1.02	0.95	95
31	0.25	1.37	6.14	0.76	1.03	0.99	85	0.23	1.26	5.59	0.80	1.02	1.00	85	0.27	1.47	2.13	0.80	0.99	0.92	83
32	0.69	3.04	4.60	0.60	1.00	1.00	55	0.34	1.50	8.29	0.53	1.01	1.14	55	0.34	1.48	4.36	0.52	1.01	0.95	63
33	0.23	1.30	5.77	0.18	1.04	1.04	36	0.27	1.49	5.46	0.25	1.02	1.05	36	0.23	1.29	6.43	0.23	0.99	0.92	75

subtracted frames have been co-added to averaged 2D spectra and then the 1D spectra, which have been used to derive the spectroscopic redshifts, have been obtained extracting and summing up the lines with higher S/N using the task `SCOPY`.

The 1D reduced spectra are showed in Figure 2. They are plotted in rest-framed wavelength from ~ 3600 to ~ 5600 Å and units of normalized flux (each spectrum has been divided by its median). The spectra are vertically shifted for better visualization. Vertical red dotted lines show absorption spectral features typical of an old stellar population.

3.2. TNG spectroscopy

The 20 spectra of UCMG candidates in the UCMG_TNG_2017 and UCMG_TNG_2018 samples have been collected

using the Device Optimized for the Low REsolution (DOLORES) spectrograph mounted on the 3.5m TNG, during 6 nights in 2017 and 2018 (PI: N.R. Napolitano, ID: A34TAC_22 and A36TAC_20). The instrument has a $2k \times 2k$ CCD detector with a pixel scale of 0.252 arcsec/pixel. The observations for both subsamples have been carried out with the LR-B grism with dispersion of 2.52 Å/pixel and resolution of 585 (calculated for a slit width of 1''), covering the wavelength range from 4000 to 8000 Å. As in the previous case, we have obtained from 1 to 5 single exposures per target, each with exposure time ranging between 600 and 1200 seconds. Following T18, the DOLORES 2D spectra have been flat-fielded, sky-subtracted and wavelength calibrated using the HgNe arc lamps. Then, the 1D spectra have been extracted

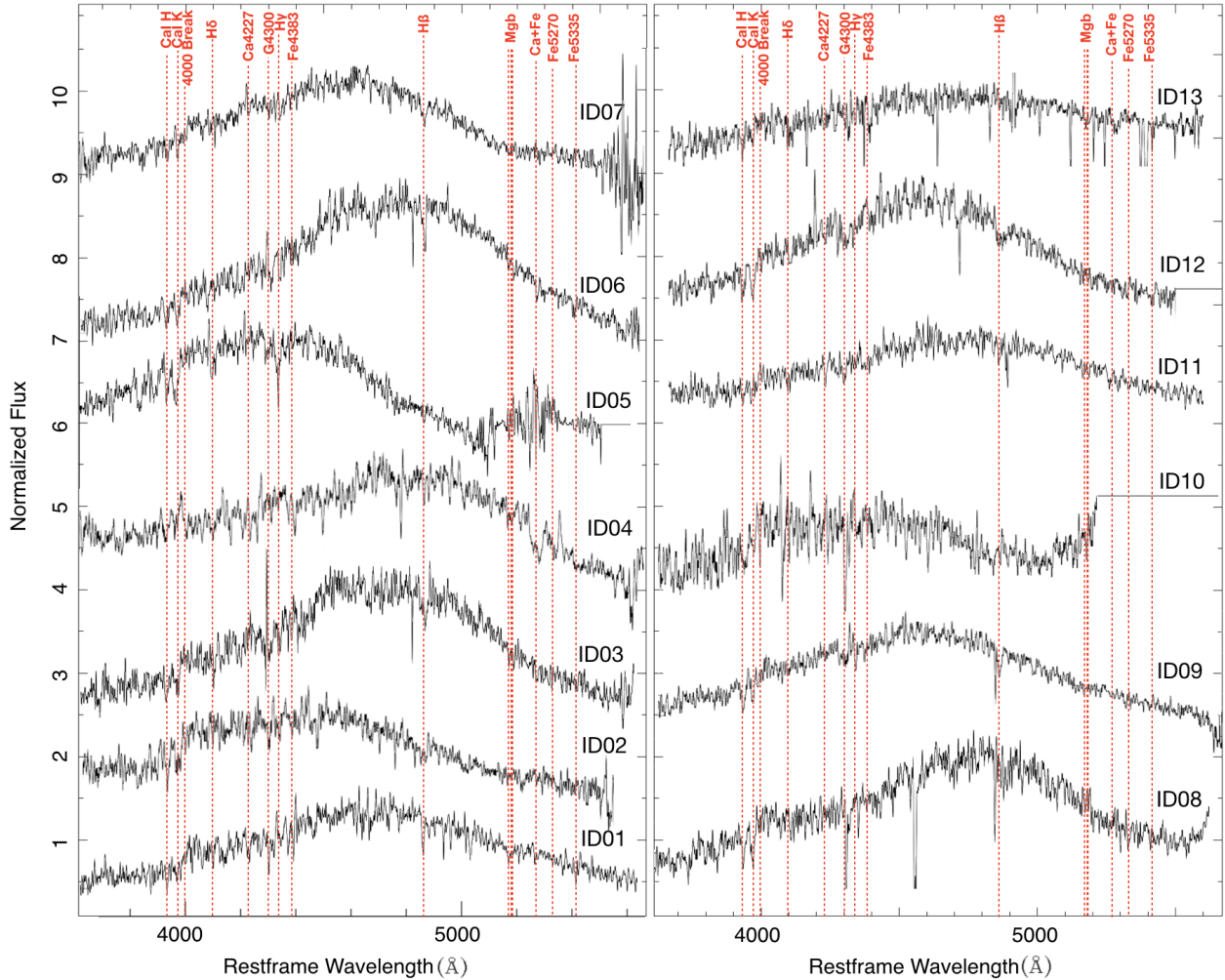


Figure 2. Spectra of the 13 candidates observed in our spectroscopic campaign with INT (UCMG_INT_2017), for which we obtain a spectroscopic redshift estimation. The spectra are plotted in ascending order of ID, which is reported above each corresponding spectrum, and refers to the IDs in Table 3. We only show the wavelength region that was used to derive the redshift and to compute the velocity dispersion. This region includes some of the most common stellar absorption lines such as Ca-H, Ca-K, Balmer lines (H_δ , H_γ and H_β), Mgb, and Fe lines. The spectra are plotted in rest-framed wavelength, in unit of normalized flux (each spectrum has been divided by its median) and they are vertically shifted for better visualization. In some cases, when the red part of the spectrum was particularly noisy, we cut it out to improve the figure layout.

by integrating over the source spatial profile. All these procedures have been performed using the same standard IRAF tasks, as explained in Section 3.1. The TNG spectra are showed in Figures 3 and 4, using the same units and scale of Figure 2. Similarly to the previous case, the main stellar absorption features are highlighted with vertical red dotted lines.

3.3. Spectroscopic signal-to-noise ratio determination

To calculate the signal-to-noise ratio (S/N_{spec}) of the integrated spectra we use the IDL code DER_SNR⁸. The

code estimates the derived S/N from the flux under the assumptions that the noise is uncorrelated in wavelength bins spaced two pixels apart and that it is approximately Gaussian distributed. The biggest advantages of using this code are that it is very simple and robust and, above all, it computes the S/N from the data alone. In fact, the noise is calculated directly from the flux using the following equation:

$$N = \frac{1.482602}{\sqrt{6} \times \langle |2S(i) - S(i-2) - S(i+2)| \rangle} \quad (2)$$

⁸ The code is written by Felix Stoehr and published on the ST-ECF Newsletter, Issue num. 42. The software is avail-

able here: www.stecf.org/software/ASTROsoft/DER_SNR/; the Newsletter can be found here: www.spacetelescope.org/about/further_information/stecfnewsletters/hst_stecf_0042/.

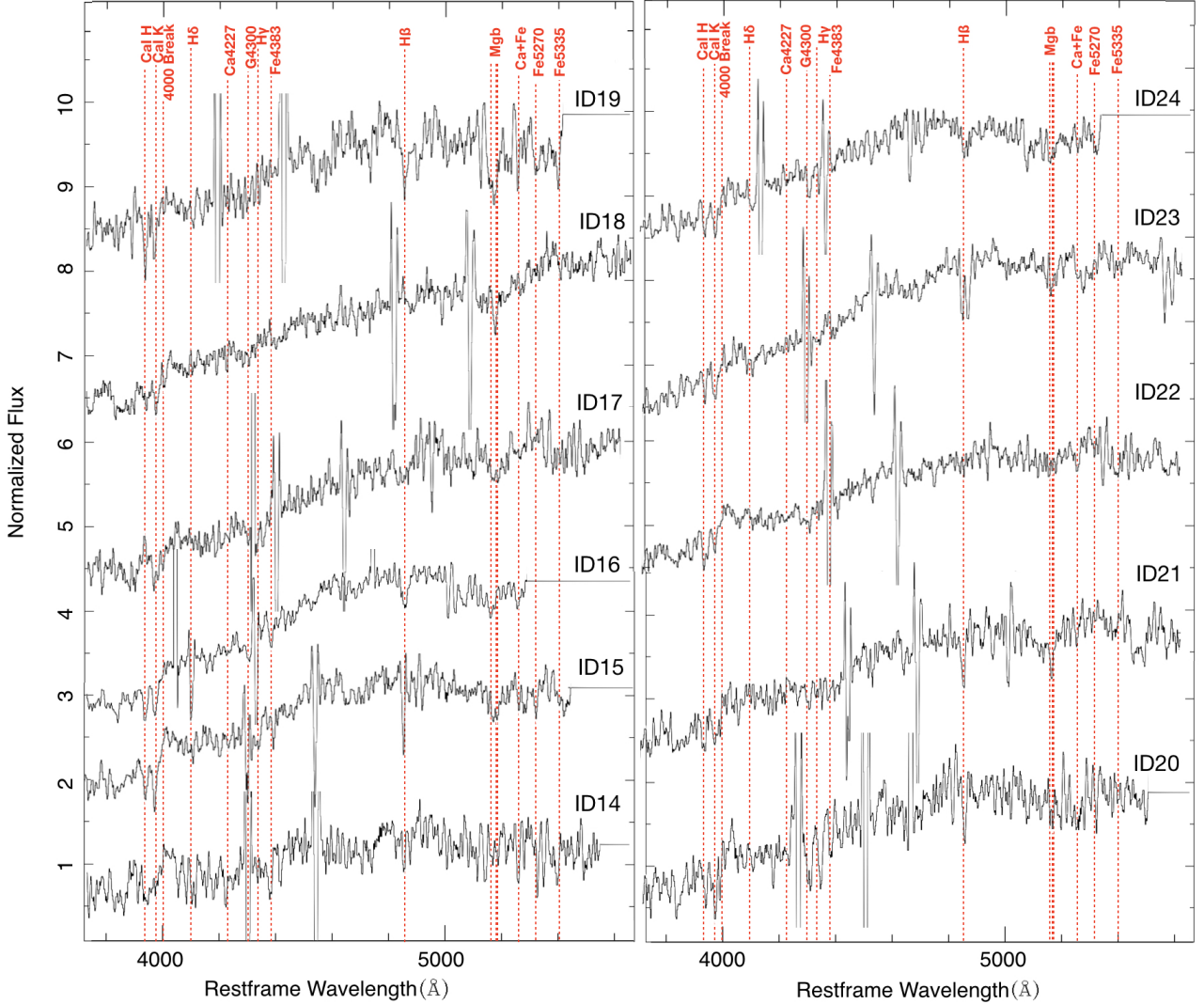


Figure 3. Same as Figure 2, but for the 11 candidates observed in our spectroscopic campaign with TNG (UCMG_TNG_2017), for which we obtain a spectroscopic redshift estimation.

where S is the signal (taken to be the flux of the continuum level), the index i runs over the pixels, and the “ $\langle \rangle$ ” symbol indicates a median calculation done over all the non-zero pixels in the restframe wavelength range 3600 – 4600 Å, which is the common wavelength range for all the spectra, including the T18 ones, for which we determine, in the next section, also the velocity dispersion. We note that these signal-to-noise ratio estimates have to be interpreted as lower limit for the whole spectrum, since they are calculated over a rather blue wavelength range, whereas the light of early-type galaxies is expected to be strong in redder regions. This arises clearly from the comparison of these S/N_{spec} with the ones we will describe in the next section, which are computed, for each galaxy, over the region used for the kinematic fit and are systematically larger. Both of them will be

used in Section 4.4 as one of the proxy of the reliability of the velocity dispersion (σ) measurements.

3.4. Redshift and velocity dispersion measurements

Redshift and velocity dispersion values have been measured with the Optimised Modelling of Early-type Galaxy Aperture Kinematics pipeline (OMEGA-K, D’Ago et al. 2018), a Python wrapper based on the Penalized Pixel-Fitting code (PPXF, Cappellari 2017).

OMEGA-K comprises a graphical user interface (PPGUI, written by G. D’Ago and to be distributed soon) that allows the user to visualize and inspect the observed spectrum in order to easily set the PPXF fitting parameters (i.e., template libraries, noise level, polynomials, fit wavelength range and custom pixel masks). We use PPGUI to restframe the spectra and

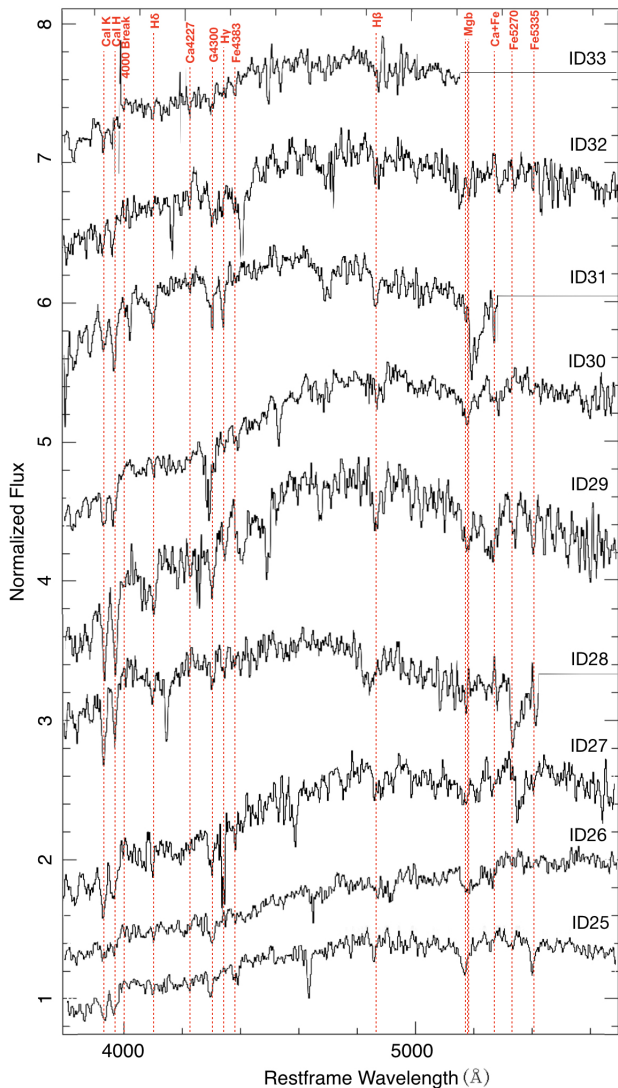


Figure 4. Same as Figure 2, but for the 9 candidates observed in our spectroscopic campaign with TNG (UCMG_TNG_2018), for which we obtain a spectroscopic redshift estimation.

obtain a first guess of the redshift, initially based on the z_{phot} .

The aim of OMEGA-K is to automatically retrieve an optimal pixel mask and noise level (1σ noise spectrum) for the observed spectrum, and to find a robust estimate of the galaxy kinematics together with its uncertainties by randomizing the initial condition for PPXF and running it hundreds of times on the same observed spectrum, to which a Gaussian noise is randomly added.

As templates for the fitting we use a selection of 156 MILES simple single stellar population (SSP) models from Vazdekis et al. (2010), covering a wide range of metallicities ($0.02 \leq Z/Z_{\odot} \leq 1.58$) and ages (between 3 Gyr and 13 Gyr). We also perform the fitting using sin-

gle stars (268 empirical stars from MILES library, uniformly sampling effective temperature, metallicity and surface gravity of the full catalogue of templates) and also including templates with ages < 3 Gyr.

The results do not change and are always consistent within the errors, demonstrating that the choice of the templates does not influence the fitting results.⁹ Finally, an additive polynomial is also applied in order to take into account possible template shape and continuum mismatches and correct for imperfect sky subtraction or scattered light.

For a general description of the OMEGA-K pipeline, we refer the reader to above mentioned reference (see also D’Ago et al. 2018) and the paper in preparation (D’Ago et al. in prep.). Here, we list the main steps of the OMEGA-K run specifically adopted for this work on a single observed spectrum:

1. the observed spectrum and the template libraries are ingested;
2. the optimal 1σ noise spectrum and pixel mask are automatically tuned;
3. 256 Monte Carlo re-samplings of the observed spectrum using a random Gaussian noise from the 1σ noise spectrum are produced;
4. 256 sets of initial guesses (for the redshift and the velocity dispersion) and of fitting parameters (additive polynomial degree, number of momenta of the line-of-sight velocity distribution to be fitted, random shift of the fitting wavelength range) are produced in order to allow for a complete bootstrap approach within the parameter space, and to avoid internal biases in the pipeline;
5. 256 pPXF runs are performed in parallel and the results from each run are stored (outliers and too noisy reproductions of the observed spectra are automatically discarded);
6. the final redshift and velocity dispersion for each observed spectrum, together with their error are defined as the mean and the standard deviation of the result distribution from the accepted fits.

Among the 257 fits performed on each spectrum (256 from the OMEGA-K bootstrap stage, plus the fit on the original observed spectrum), we discard the ones

⁹ We note that the stellar templates are used only to infer the kinematics, i.e. to measure the shift and the broadening of the stellar absorption lines. Given the low S/N of our spectra, we do not perform any spectroscopic stellar population analysis.

for which the best fit fails to converge or the measured kinematics is unrealistically low or unrealistically high. As a lower and upper limit on the velocity, we choose thresholds of 110 and 500 km s^{-1} , respectively. The low limit is slightly smaller than the typical velocity scale of the instrument, which we measure to be $\sim 120 \text{ km s}^{-1}$. On the other hand, we used 500 km s^{-1} as a high upper limit in order to incorporate any possible source of uncertainty related to the pipeline, without artificially reduce the errors on our estimates.

We define the success rate (SR) as the ratio between the number of accepted fits over the total 257 attempts.

Finally, OMEGA-K derives a mean spectrum of the accepted fits and performs a measurement of the S/N on its residuals ($(S/N)_{\text{O-K}}$). D’Ago et al. (2018) showed, using mock data, a large sample of SDSS spectra and the entire GAMA DR3 spectroscopic database, that kinematics values with $\text{SR} > 65\%$ and $(S/N)_{\text{O-K}} > 5/\text{px}$ can be considered totally reliable. This S/N ratio is also consistent with what found in Hopkins et al. (2013, and reference therein).

The uncertainties on our measures are unfortunately very large. To assess the effect of such large errors on our findings, we separate the UCMGs in two groups: those with “high-quality” (HQ) velocity dispersion measurements and those with “low-quality” (LQ) ones. For this purpose, we use a combination of three “quality criteria”: the aforementioned SR, the spectral S/N calculated on a common wavelength range covered by all the spectra (see Section 3.3) and the $(S/N)_{\text{O-K}}$ from the OMEGA-K pipeline (calculated over different wavelength ranges for different spectra). We visually inspect the spectra and their fit one by one in order to set reliable thresholds for these criteria. We set-up the following quality low limits: $\text{SR} = 0.3$, $S/N_{\text{spec}} = 3.5$ and $(S/N)_{\text{O-K}} = 6.5/\text{px}$. We then classify as HQ objects, the ones above these limits.

In Figure 5 we show two examples of the ppxf fit obtained with OMEGA-K on the spectra of two different objects from the sample of the 33 UCMG candidates for which we obtain new spectroscopy in this paper. These two spectra are representative of the full sample since they have been observed with two different instruments and one is classified as high-quality while the other as low-quality. The upper panel shows the galaxy KIDS J090412.45-001819.75 (ID = 15), from the UCMG_TNG_2017 sample, which is classified as HQ and has a large velocity dispersion ($\sigma = 412 \pm 81 \text{ km s}^{-1}$). Instead, the lower panel shows the spectrum of the galaxy KIDS J085700.29-010844.55 (ID = 1), which belongs to UCMG_INT_2017. This object, classified as LQ, has a rel-

atively lower velocity dispersion ($\sigma = 187 \pm 85 \text{ km s}^{-1}$) and is one of the worse cases with very low spectral S/N.

In addition to the 33 new UCMG candidates presented in this paper, we also apply the same kinematics procedure to the 28 UCMG candidates from T18, 6 observed with TNG and 22 with NTT, to which we refer to as UCMG_TNG_T18 and UCMG_NTT_T18 sample, respectively.

In general, the velocity dispersion values from OMEGA-K are derived from 1D spectra using various slit widths and extracted using different number of pixels along the slit length. This means that the velocity dispersion values are computed integrating light in apertures with different sizes. The ranges of aperture and slit widths for the new 33 objects presented here and the 28 UCMG candidates from T18 are $1.8'' - 3.2''$ and $1.2'' - 2''$, respectively. This is not an ideal situation if we want to compare velocity dispersion values among different systems and use these measurements to derive scaling relations. We will come back to this specific topic in Section 4.4. Briefly, in order to uniform the estimates, and correct the velocity dispersion values for the different apertures, we first convert the rectangular aperture adopted to extract the UCMG 1D spectra to an equivalent circular aperture of radius $R = 1.025\sqrt{(\delta x \delta y / \pi)}$, where δx and δy are the width and length used to extract the spectrum¹⁰. Then, we use the average velocity dispersion profile in Cappellari et al. (2006), to extrapolate this equivalent velocity dispersion to the effective radius.

Table 3 and Table 4 list the results of the fitting procedure for our sample and that of T18. We report the measured spectroscopic redshifts and the velocity dispersion values, each with associate error, the velocity dispersion values corrected to the effective radii (σ_e) and, the equivalent circular apertures for the whole sample of 61 UCMGs. We also present the photometric redshifts to provide a direct comparison with the spectroscopic. Finally, the four following columns indicate the three parameters we use to split the sample in high- and low-quality and the resulting classification for each object.

In addition, we correct the value of the spectroscopic redshift for the object with ID number 46 (corresponding to ID 13 in T18) respect to the wrong one reported in T18. Although this changes the value of R_e the result of the spectroscopic validation remains unchanged and the galaxy is still a confirmed UCMG. The 28 galaxies from T18 are reported in the same order as the previous

¹⁰ The same formula was adopted in Tortora et al. (2014), but reported with a typo in the printed copy of the paper.

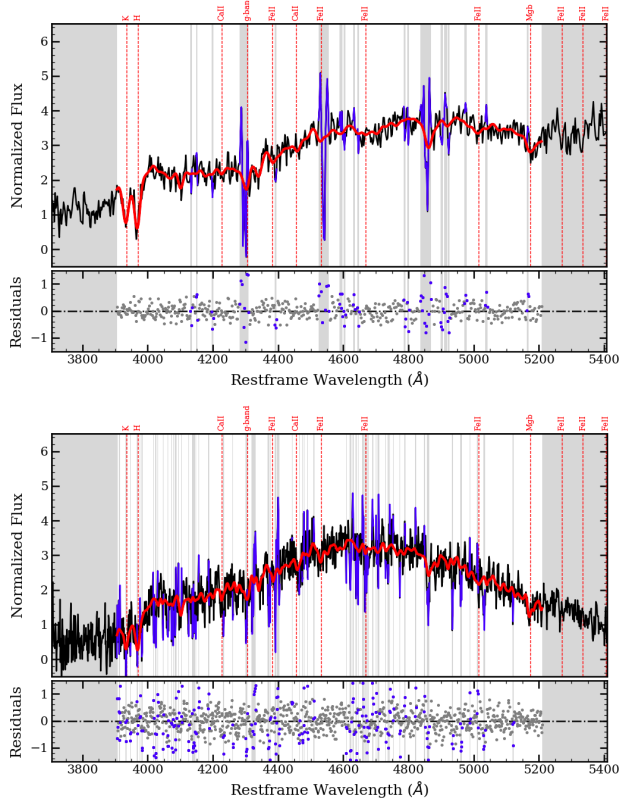


Figure 5. Two examples of ppxf fits obtained with OMEGA-K on the spectra of two different UCMGs, one of the best HQ system and one of the worse LQ system, thus representative of the whole sample, observed with two different telescopes. For each panel we plot the galaxy spectrum in black, the best template fit in red and the regions excluded from the fit as blue lines. We note that the fit is performed only outside the gray shaded regions. Finally, we highlight stellar absorption lines in red and show the residuals of the plot below each panel.

paper but continuing the numeration (in terms of ID) of this paper.

4. RESULTS

Although the photometric redshifts generally reproduce quite well the spectroscopic ones (Figure 6), small variations in z_{phot} can induce variations in R_e and M_* large enough to bring them outside the limits for our definition of UCMG (i.e., it might happens that $R_e > 1.5$ kpc and/or $M_* < 8 \times 10^{10} M_\odot$). Thus, having obtained the spectroscopic redshifts, we are now able to re-calculate both R_e and M_* , and find how many candidates are still ultra-compact and massive according to our definition.

Following the analysis of T18, in the next subsections we study the success rate of our selection and systematics in UCMG abundances. We then quantify the UCMG number counts, comparing our new results with the ones

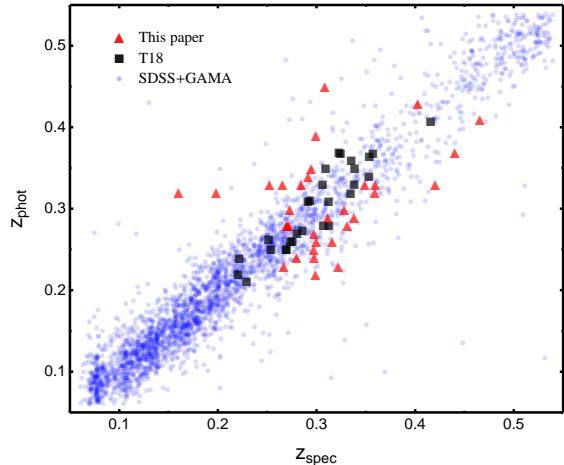


Figure 6. Spectroscopic vs photometric redshifts. Red triangles are for the new sample of 33 UCMG candidates analyzed in this paper with redshifts measured from observations at INT and TNG. Black squares are relative to the set of 28 UCMG KiDS candidates with redshifts measured from observations at TNG and NTT presented in T18. Blue points are for a parent sample of galaxies with SDSS and GAMA spectroscopy (extracted from KiDS_SPEC), used by Cavuoti et al. (2015b) as a test set for the validation of the photometric redshift determination. We find a good agreement with the 1-to-1 relation for most of the objects in For all the all the datasets.

in the literature. We finally show where the final sample of spectroscopically confirmed objects (i.e., the ones presented in T18 plus the ones presented here) locates on the $M_* - \sigma$ plane, to establish some basis for future analysis of the scaling relation.

4.1. UCMGs validation

In Figure 6 we compare the spectroscopic redshifts measured for the candidates of this paper with the photometric redshift values (red triangles). The results are also compared with the 28 UCMG from T18 (black squares) and with a sample of galaxies with SDSS and GAMA spectroscopy (blue points) from KiDS-DR2 (Cavuoti et al. 2015b). As one can clearly see from the figure, the distribution of the new redshifts is generally consistent with what found using the full sample of galaxies included in KiDS-DR3, on average reproducing well the spectroscopic redshifts.

The agreement on the redshifts can be better quantified by using statistical indicators (Cavuoti et al. 2015b; T18). Following the analysis of T18, we define this quantity:

$$\Delta z \equiv \frac{z_{\text{spec}} - z_{\text{phot}}}{1 + z_{\text{spec}}}, \quad (3)$$

then we interpret the scatter as the standard deviation of Δz , and bias as the absolute value of the mean of

Table 3. Results of the fitting procedure on the spectra belonging to the three observational runs presented here: UCMG_INT_2017, UCMG_TNG_2017, UCMG_TNG_2018. The columns from left to right list: the galaxy ID, the photometric redshift, the measured spectroscopic redshift with its error, the measured velocity dispersion in km s^{-1} with its error, the corrected velocity dispersion to the effective radius, the equivalent circular aperture in arcsec. Finally, in the final four columns, we also report the success rate, the signal-to-noise ratio per pixel calculated in the range 3600 – 4600 Å, the signal-to-noise ratio per pixel calculated over the region used for the fit by OMEGA-K, and the quality level of the velocity dispersion estimates, based on these three quality parameters.

ID	z_{phot}	$z_{\text{spec}} \pm \Delta z_{\text{spec}}$	$\sigma \pm \Delta\sigma$	σ_e	Aperture	SR	$(S/N)_{\text{spec}}$	$(S/N)_{\text{O-K}}$	Quality level
1	0.28	0.2696 ± 0.0002	197 ± 85	211	0.97	0.62	1.99	6.13	LQ
2	0.26	0.3158 ± 0.0002	195 ± 52	210	0.97	0.77	3.21	5.69	LQ
3	0.26	0.2995 ± 0.0003	268 ± 76	291	1.21	0.79	2.50	6.19	LQ
4	0.45	0.3084 ± 0.0005	234 ± 86	281	0.97	0.30	2.18	4.23	LQ
5	0.37	0.4401 ± 0.0003	142 ± 33	161	0.97	0.07	4.00	6.87	LQ
6	0.22	0.2988 ± 0.0002	202 ± 48	217	1.21	0.75	2.42	7.27	LQ
7	0.23	0.3221 ± 0.0002	208 ± 84	224	0.97	0.15	2.96	6.71	LQ
8	0.24	0.2976 ± 0.0002	241 ± 100	257	0.97	0.59	3.06	6.31	LQ
9	0.34	0.2915 ± 0.0001	227 ± 84	251	0.97	0.21	4.07	6.04	LQ
10	0.32	0.3590 ± 0.0004	265 ± 100	293	0.97	0.12	2.00	2.05	LQ
11	0.24	0.2797 ± 0.0003	260 ± 94	286	0.97	0.85	1.40	4.58	LQ
12	0.28	0.3312 ± 0.0002	202 ± 59	218	0.97	0.73	2.70	6.76	LQ
13	0.23	0.2668 ± 0.0007	259 ± 113	274	0.97	0.23	1.77	2.89	LQ
14	0.35	0.2946 ± 0.0003	340 ± 99	369	0.94	0.66	2.01	3.97	LQ
15	0.27	0.2974 ± 0.0002	412 ± 81	451	1.07	0.69	6.90	13.25	HQ
16	0.33	0.3594 ± 0.0001	268 ± 84	292	1.01	0.84	6.87	14.32	HQ
17	0.33	0.2656 ± 0.0006	321 ± 93	347	1.01	0.43	1.95	8.20	LQ
18	0.32	0.1586 ± 0.0002	253 ± 92	276	1.01	0.70	2.93	12.76	LQ
19	0.30	0.3281 ± 0.0002	230 ± 91	251	1.18	0.30	2.97	6.27	LQ
20	0.30	0.2728 ± 0.0003	331 ± 92	361	1.12	0.21	2.85	5.58	LQ
21	0.33	0.2523 ± 0.0003	323 ± 95	366	1.12	0.85	2.62	9.93	LQ
22	0.28	0.2719 ± 0.0002	355 ± 99	413	1.18	0.66	5.91	12.72	HQ
23	0.25	0.2971 ± 0.0002	407 ± 56	443	1.12	0.79	6.18	17.38	HQ
24	0.33	0.3491 ± 0.0002	194 ± 64	215	1.07	0.23	5.79	11.15	LQ
25	0.28	0.2703 ± 0.0002	274 ± 57	298	1.12	0.91	6.80	18.11	HQ
26	0.32	0.1984 ± 0.0002	287 ± 57	316	1.18	0.89	3.96	17.92	HQ
27	0.33	0.2843 ± 0.0002	241 ± 53	267	1.23	0.91	5.08	15.85	HQ
28	0.33	0.4203 ± 0.0002	172 ± 63	191	1.18	0.02	6.59	11.69	LQ
29	0.29	0.3116 ± 0.0002	164 ± 39	177	1.01	0.52	7.74	15.65	HQ
30	0.39	0.2994 ± 0.0002	289 ± 52	319	1.12	1.00	8.53	24.59	HQ
31	0.41	0.4655 ± 0.0001	253 ± 57	280	1.18	0.98	9.18	18.13	HQ
32	0.29	0.3382 ± 0.0003	277 ± 85	301	1.18	0.88	3.51	9.73	HQ
33	0.43	0.4028 ± 0.0003	299 ± 91	335	1.28	0.84	4.96	9.16	HQ

Δz . We find a bias of 0.0008 and a scatter of 0.0516 for our 33 systems. These estimates show a larger scatter of the new sample with respect to the sample of galaxies in T18, for which we found a bias of 0.0045 and a standard deviation of 0.028.

Since we use a new stellar mass calculation set-up with respect to the one in T18, we recalculate sizes and masses, with both z_{phot} and z_{spec} for the final, total, spectroscopic sample of 61 systems. The results are pro-

vided in Table 5 and Table 6, where we also report, in the last column, the UCMGs spectral validation.

Using the face values for masses and sizes inferred from the spectroscopic redshifts, we confirm as UCMGs 19 out of 33 new UCMG candidates. This corresponds to a success rate of 58%, a number which is fully consistent with the 50–60% estimate found in T18. Moreover, using the new mass set-up, 27 out the 28 objects of T18 are still UCMG candidates according to the mass selection using

Table 4. Same as Table 3, but for the samples UCMG_TNG_T18 and UCMG_NTT_T18.

ID	z_{phot}	$z_{\text{spec}} \pm \Delta z_{\text{spec}}$	$\sigma \pm \Delta\sigma$	σ_e	Aperture	SR	$(S/N)_{\text{spec}}$	$(S/N)_{\text{O-K}}$	Quality level
34	0.29	0.3705 ± 0.0001	361 ± 63	392	1.12	0.98	15.05	22.41	HQ
35	0.22	0.2175 ± 0.0004	404 ± 101	446	1.59	0.31	7.68	14.62	HQ
36	0.35	0.4078 ± 0.0002	366 ± 79	412	1.33	0.93	6.70	14.33	HQ
37	0.31	0.3341 ± 0.0002	218 ± 54	242	1.12	0.92	7.84	17.82	HQ
38	0.42	0.3988 ± 0.0003	390 ± 71	448	1.01	0.75	5.33	12.67	HQ
39	0.36	0.3190 ± 0.0004	226 ± 65	245	1.01	0.82	4.14	10.20	HQ
40	0.20	0.3019 ± 0.0002	432 ± 41	464	0.69	0.73	2.09	6.75	LQ
41	0.35	0.3853 ± 0.0001	211 ± 40	223	0.69	0.98	3.69	10.92	HQ
42	0.28	0.2367 ± 0.0003	225 ± 34	235	0.69	1.00	2.38	9.30	LQ
43	0.29	0.2801 ± 0.0001	196 ± 39	214	0.69	0.94	2.77	9.55	LQ
44	0.31	0.2789 ± 0.0001	218 ± 34	235	0.69	1.00	3.67	12.46	HQ
45	0.27	0.2888 ± 0.0001	195 ± 46	216	0.69	0.94	3.09	9.30	LQ
46	0.31	0.3618 ± 0.0053	181 ± 68	196	0.69	0.09	1.39	4.08	LQ
47	0.25	0.2622 ± 0.0003	340 ± 53	363	0.69	0.99	2.31	7.65	LQ
48	0.27	0.2949 ± 0.0003	280 ± 50	295	0.69	1.00	3.79	10.53	HQ
49	0.28	0.2974 ± 0.0001	142 ± 22	149	0.69	0.58	3.54	10.01	HQ
50	0.29	0.3188 ± 0.0001	387 ± 63	408	0.69	0.96	3.88	11.85	HQ
51	0.34	0.3151 ± 0.0001	154 ± 29	166	0.69	0.66	3.82	11.69	HQ
52	0.22	0.2124 ± 0.0001	252 ± 43	265	0.69	1.00	1.64	9.19	LQ
53	0.25	0.2578 ± 0.0002	183 ± 48	194	0.69	0.68	2.37	9.73	LQ
54	0.34	0.3024 ± 0.0009	214 ± 66	226	0.69	0.70	1.97	4.14	LQ
55	0.31	0.3667 ± 0.0001	244 ± 30	262	0.69	1.00	4.99	13.10	HQ
56	0.32	0.4070 ± 0.0001	322 ± 54	342	0.69	1.00	4.82	10.60	HQ
57	0.33	0.2612 ± 0.0001	219 ± 44	233	0.69	0.99	3.00	10.88	LQ
58	0.27	0.2818 ± 0.0002	218 ± 64	227	0.69	0.92	2.41	7.38	LQ
59	0.23	0.2889 ± 0.0002	209 ± 52	221	0.69	0.95	2.80	9.99	LQ
60	0.34	0.3393 ± 0.0001	155 ± 30	167	0.69	0.73	4.59	10.78	HQ
61	0.31	0.2889 ± 0.0001	220 ± 33	236	0.69	1.00	2.47	8.67	LQ

the photometric redshift values, and 18 are spectroscopically confirmed UCMGs. This corresponds to a success rate of 67%. In total, we confirmed 37 out of 61 UCMGs, with a success rate of 60%. Considering only the new 19/33 confirmed UCMGs, we find a bias of 0.016 and a scatter of 0.037 in the $z_{\text{phot}} - z_{\text{spec}}$ plot. This reflects the expectation that the objects with a larger scatter after the validation do not result compact and massive anymore according to our formal definition.

A very important point to stress here is that in the validation process we do not propagate the error on the photometric and spectroscopic redshifts into masses and sizes errors. We simply use the face values and include/exclude galaxies on the basis of the resulting nominal size and mass values. This might lead us to loose some galaxies at the edges, but it simplifies the analysis of the systematics, necessary to correct the number density (see Section 4.3). If we take into account the average statistical 1σ -level uncertainties for the measured effective radii and the stellar masses calculated in T18 (see

the paper), i.e. $\delta R_e \sim 20\%$ and $\delta \log_{10}(M_*/M_\odot) \sim 0.15$, we confirm as UCMGs 57 out of 61 UCMG candidates ($\sim 93\%$). If we consider, instead, the 3σ -level uncertainties, all the candidates are statistically consistent with the UCMG definition. In the following, we analyze the systematics considering the face values for R_e and M_* in the selection.

4.2. Contamination and incompleteness

One of the main aims of our spectroscopic campaigns is to quantify the impact of systematics on the UCMG photometric selection. Because of the uncertain photometric redshifts, the candidate selection: 1) includes “contaminants” (or false-positives), i.e., galaxies which are selected as UCMGs according to their photometric redshifts, but would not result ultra-compact and massive when recalculating the masses on the basis of the more accurate spectroscopic redshift values (see T16 and T18) and 2) “missed” systems (or false-negatives), i.e., those galaxies which are not selected as UCMGs accord-

Table 5. Photometric and spectroscopic parameters (redshifts, median effective radii in kpc and stellar masses) for the validation of the new samples: UCMG_INT_2017, UCMG_TNG_2017, and UCMG_TNG_2018. The last column indicates the spectral validation response: “Y” if the candidate is a confirmed UCMG, (i.e. $\log_{10}(M_*/M_\odot) > 10.9$ and $R_e < 1.5$ kpc), “N” if it is not.

ID	z		R_e		$\log_{10}(M_*/M_\odot)$		Spec.
	phot	spec	phot	spec	phot	spec	Valid.
1	0.28	0.27	1.43	1.39	11.03	11.00	Y
2	0.26	0.32	1.23	1.43	10.94	11.07	Y
3	0.26	0.30	1.36	1.51	10.92	11.21	N
4	0.45	0.31	0.35	0.28	11.29	10.83	N
5	0.37	0.44	0.71	0.79	11.32	11.24	Y
6	0.22	0.30	1.44	1.81	10.93	11.20	N
7	0.23	0.32	1.12	1.42	10.92	11.27	Y
8	0.24	0.30	1.36	1.60	10.93	11.06	N
9	0.34	0.29	1.04	0.94	10.92	10.73	N
10	0.32	0.36	0.98	1.06	11.21	11.19	Y
11	0.24	0.28	1.31	0.96	10.98	10.99	Y
12	0.28	0.33	1.30	1.45	10.95	11.07	Y
13	0.23	0.27	1.50	1.69	11.03	11.03	N
14	0.35	0.29	1.37	1.20	11.08	10.96	Y
15	0.27	0.30	1.13	1.22	11.08	11.10	Y
16	0.33	0.36	1.28	1.36	11.25	11.34	Y
17	0.33	0.27	1.47	1.28	11.16	10.97	Y
18	0.32	0.16	1.25	0.74	10.98	10.61	N
19	0.30	0.33	1.38	1.47	11.01	10.83	N
20	0.30	0.27	1.37	1.27	10.95	10.97	Y
21	0.33	0.25	0.81	0.67	10.99	10.82	N
22	0.28	0.27	0.50	0.49	11.01	10.85	N
23	0.25	0.30	1.22	1.39	11.12	11.26	Y
24	0.33	0.35	1.07	1.11	11.01	11.06	Y
25	0.28	0.27	1.30	1.27	10.97	10.94	Y
26	0.32	0.20	1.28	0.90	10.92	10.46	N
27	0.33	0.28	1.26	1.12	10.97	10.85	N
28	0.33	0.42	1.14	1.32	11.00	11.25	Y
29	0.29	0.31	1.42	1.49	10.99	10.99	Y
30	0.39	0.30	1.35	1.14	11.02	10.78	N
31	0.41	0.47	1.37	1.49	10.93	11.03	Y
32	0.29	0.34	1.48	1.65	11.06	11.18	N
33	0.43	0.40	1.30	1.24	11.31	11.24	Y

ing to their photometric redshifts, but would be selected using the spectroscopic values instead (i.e., they are real UCMGs that our selection excluded). Thus, following T18, we define the *contamination factor*, \mathcal{C}_F the inverse of the success rate discussed in the previous subsection, to account for the number of “contaminants” and the *incompleteness factor*, \mathcal{I}_F the difference between the num-

Table 6. Same as Table 5, but for the UCMG_TNG_T18 and UCMG_NTT_T18 samples.

ID	z		R_e		$\log_{10}(M_*/M_\odot)$		Spec.
	phot	spec	phot	spec	phot	spec	Valid.
34	0.29	0.37	1.43	1.68	10.97	11.35	N
35	0.22	0.22	1.28	1.27	11.12	11.11	Y
36	0.35	0.41	1.09	1.19	10.92	10.97	Y
37	0.31	0.33	1.06	1.10	10.73	10.80	N
38	0.42	0.40	0.67	0.66	10.98	10.94	Y
39	0.36	0.32	1.46	1.36	10.99	10.87	N
40	0.2	0.30	1.11	1.06	10.94	10.94	Y
41	0.35	0.39	1.45	1.54	11.37	11.43	N
42	0.28	0.24	1.47	1.32	10.91	10.84	N
43	0.29	0.28	0.81	0.80	11.01	10.99	Y
44	0.31	0.28	1.01	0.95	11.01	10.77	N
45	0.27	0.29	0.62	0.65	10.99	11.00	Y
46	0.31	0.36	0.92	1.01	10.95	10.94	Y
47	0.25	0.26	1.02	1.04	10.97	10.94	Y
48	0.27	0.29	1.29	1.36	11.04	11.09	Y
49	0.28	0.30	1.36	1.42	10.91	10.97	Y
50	0.29	0.32	1.36	1.43	11.02	11.04	Y
51	0.34	0.32	1.04	0.99	10.98	10.89	N
52	0.22	0.21	1.11	1.08	10.96	10.70	N
53	0.25	0.26	1.15	1.16	10.95	10.97	Y
54	0.34	0.30	1.47	1.37	11.03	10.93	Y
55	0.31	0.37	1.10	1.24	10.96	11.13	Y
56	0.32	0.41	1.29	1.50	11.22	11.20	Y
57	0.33	0.26	1.27	1.07	10.96	10.81	N
58	0.27	0.28	1.49	1.54	11.00	11.04	N
59	0.23	0.29	1.10	1.30	10.94	11.12	Y
60	0.34	0.34	1.05	1.05	10.99	10.99	Y
61	0.31	0.29	1.08	1.03	11.09	11.03	Y

ber of UCMG candidates using z_{spec} and z_{phot} , to estimate the incompleteness of the sample, i.e. quantifying the number of “missing” objects.

In this section we only report the average values for these factors across the full redshift range. We use instead different values calculated in different redshift bins to correct the abundances presented in Section 4.3. To estimate the fraction of contaminants, we need UCMG samples selected using the photometric redshifts, but for which we have also spectroscopic redshifts available. Thus, we evaluate \mathcal{C}_F using three different photometrically selected samples with $z_{\text{phot}} < 0.5$:

- a) the new sample of 33 UCMG candidates presented in this paper and discussed in Section 3,
- b) 27 (out of 28) UCMG candidates from T18, that satisfy the new mass and size selection based on z_{phot}

using the new set-up for stellar masses adopted here, and

- c) the sample of 50 photometrically selected galaxies introduced in Section 2.2, UCMG_PHOT_SPEC with measured spectroscopic redshifts from SDSS, GAMA and 2dFLenS, similar to the one presented in T18 but selected with the new mass set-up.

For a), the new sample of UCMGs presented in this paper, we obtain a $C_F = 1.72$ (corresponding to a success rate of 58%, see Section 4.1). Considering the samples in b) and c), we find $C_F = 1.50$ and 1.72, respectively. Joining these three samples, we collect a sample of 110 UCMG candidates, of which 68 have been validated after spectroscopy, implying a cumulative success rate of 62% or $C_F = 1.62$.

To quantify how many real UCMGs are missing from the photometric selection (incompleteness), we need to use objects with spectroscopic redshifts available from the literature. Thus, to determine \mathcal{I}_F , we use UCMG_SPEC: the sample of spectroscopically validated UCMGs with spectroscopic redshifts from SDSS, GAMA and 2dFLenS. This sample updates and complements the one already presented in T18 (Tables C1 and C2) and consists of 54 galaxies between $0.15 < z < 0.5$. The basic photometric and structural parameters for these UCMGs in the spectroscopically selected sample is given in the Appendix. Only 29 out of 54 galaxies, i.e., 54%, would have been selected as candidates using z_{phot} instead of z_{spec} , which corresponds to $\mathcal{I}_F = 1.86$.

Having estimated contaminants and incompleteness, we can now obtain the correction factor for the number counts, as \mathcal{I}_F/C_F . In conclusion, we find that the true number counts for UCMGs at $z < 0.5$ would be $\sim 15\%$ higher than the values one would find in a photometrically selected sample, on average. This is valid for the whole redshift range we consider here. In the next section, instead, we calculate a correction in each single redshift bin to minimize the errors on number counts.

4.3. UCMG number counts

UCMG number counts are calculated following the procedure outlined in T18. For completeness, we report here some details.

Taking into account the two systematic effects discussed in Section 4.2, we correct the number counts of the 1221 candidates in UCMG_FULL. In Figure 7 we plot the uncorrected and corrected counts as open squares/dashed line and filled squares/solid line respectively. We bin galaxies in four redshift bins ($z \in (0.15, 0.2), (0.2, 0.3), (0.3, 0.4), (0.4, 0.5)$) and normalize to the comoving volume corresponding to the observed

KiDS effective sky area of 333 deg^2 (see T18 for further details). The errors on number counts take into account fluctuations due to Poisson noise, as well as those due to large-scale structure, i.e. the cosmic variance¹¹. For this calculation, we use the number of spectroscopically validated UCMGs in each redshift bin. The uncertainties in stellar mass and effective radius measurements are also included in the error budget (as discussed in T18). The number density expectation for the KiDS tile centered on the COSMOS field is also plotted as a gray star. Increasing the number of confirmed objects, thanks to the validation presented in this paper, we are able to reduce the error budget from cosmic variance and Poisson noise of 5 – 25%, in the four redshift bins.

The final result is fully consistent with the one found in T18 and shows a decrease of number counts with cosmic time, from $\sim 9 \times 10^{-6} \text{ Mpc}^{-3}$ at $z \sim 0.5$, to $\sim 10^{-6} \text{ Mpc}^{-3}$ at $z \sim 0.15$. The number of UCMGs decreases by a factor of ~ 9 in about 3 Gyr.

Following T18, we also compare our findings to lower redshift analyses (Trujillo et al. 2009; Poggianti et al. 2013c; Taylor et al. 2010; Trujillo et al. 2014; Saulder et al. 2015), and to other intermediate redshifts studies (Damjanov et al. 2014, BOSS; Damjanov et al. 2015a, COSMOS). The reader is referred to T18 for a more detailed comparison between the different literature results and a detailed discussion on the impact of the different thresholds and selection criteria that different publications have used. In particular, we do not plot here the results obtained in Charbonnier et al. (2017) and Buitrago et al. (2018), since these authors use less restrictive size criterion ($R_e < 2 \text{ kpc}$). However, including these results, we would have a perfect agreement with number densities reported in Charbonnier et al. (2017) in terms of normalization and evolution with redshift.

Finally, we also make a comparison with the results presented in Quilis & Trujillo (2013), who have determined the evolution of the number counts of compact galaxies from Semi-analytical models, based on the Millennium N-body simulations by Guo et al. (2011, 2013). They define “relic compacts” those galaxies with mass changing less than 10 and 30 per cent, from $z \sim 2$. The redshift evolution predicted by these simulations is milder than that obtained with our data, which are in agreement with COSMOS selection at $z \sim 0.5$ instead (Damjanov et al. 2015a), and with the most recent number density determination in local environment made by Trujillo et al. (2014).

¹¹ These sources of errors are calculated with the public cosmic variance calculator available at <http://casa.colorado.edu/~simstrenti/CosmicVariance.html> (Trenti & Stiavelli 2008)

In the bottom panel of Figure 7 we directly compare our uncorrected and corrected (for systematics) counts with those found in T18, where we used two different setups for the stellar mass derivation, both of them without any constraints on ages and metallicity (which we instead set here in this paper, as described in Section 2.1). In particular, the MFREE masses (red lines and points in the plot) do not include zero-point calibration errors, while MFREE-zpt ones (blue points) include such contribution. Our results are in a good agreement with the reference T18 results assuming MFREE, and consistent within 2σ with the T18 results assuming MFREE-zpt.

It is important to remark that in Figure 7 we obtain number counts for all the UCMGs, without any distinction between relics (old stellar population) and non relics (young stellar population). Unfortunately the spectra obtained here and in our previous runs (T18) do not reach a signal-to-noise high enough to allow us to perform an in-depth stellar population analysis. This is however a *conditio-sine qua non* to isolate these compact and massive galaxies whose stellar population is as old as the Universe and has been formed “in situ” during the first phase of the two-phase formation scenario (Oser et al. 2010). We will thus postpone this more detailed analysis and the redefinition of the obtained number densities to a future publication where we will remove the non-relic contaminants thanks to spectroscopic stellar population modeling.

4.4. Relationship between stellar mass and velocity dispersion

The correlation between luminosity (or stellar mass) and velocity dispersion in elliptical galaxies is a well established scaling relation (Faber et al. 1976; Hyde et al. 2009). The location of UCMGs in a mass–velocity dispersion diagram ($M_* - \sigma$) can give remarkable insights on their intrinsic properties (Saulder et al. 2015). Indeed, given the compact sizes of UCMGs, the virial theorem predicts larger velocity dispersions with respect to normal-sized galaxies of similar mass. This has also been directly confirmed with deep spectroscopy of a handful of these objects at high redshift (vanDokkum et al. 2009; Toft et al. 2012) and of the three local relics (Ferré-Mateu et al. 2017). Therefore, UCMGs should segregate in this parameter space, having a mass–velocity dispersion correlation that deviates from the one of normal-size galaxies. Also, being this $M_* - \sigma$ relation intimately connected to the assembly of baryons and dark matter, it can also provide important constraints on our understanding of the formation and evolution of these systems. This might be particularly important in the specific case of relics.

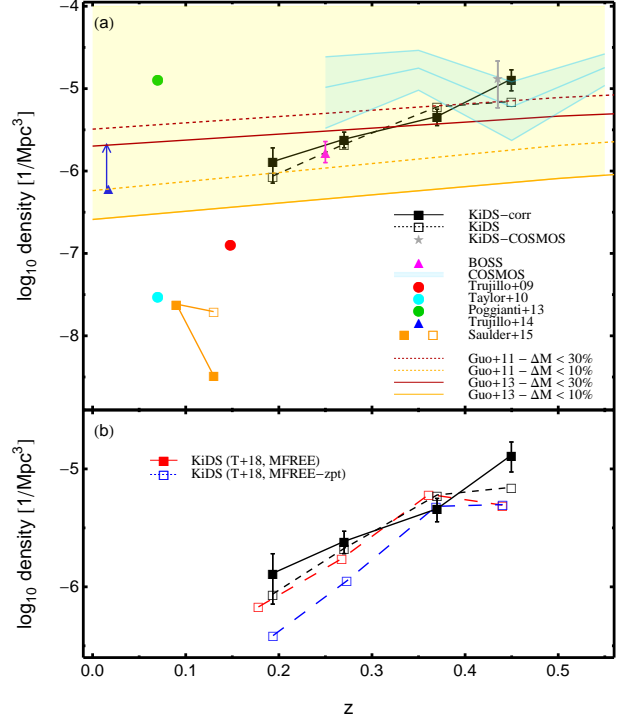


Figure 7. *Panel a.* Filled (open) black squares, with solid (dashed) line, quoted as KiDS-corr(KiDS) in the legend, plot the number density after (before) correction for systematics, for the selected sample assuming reference masses. Error bars denote 1σ uncertainties, taking into account Poisson noise, cosmic variance and errors on M_* and R_e (see the text for more details). The gray star is for the UCMG candidates at $z < 0.5$ found in the tile KIDS_150.1.2.2 centered on COSMOS field. Other colored symbols are number density obtained from other papers, as described in the caption. *Panel b.* Number counts obtained here are compared with those presented in T18, named MFREE and MFREE-zpt, see the text for more details.

In this section we present a preliminary result on the $M_* - \sigma$ relation, based on the velocity dispersion measurements presented in Section 3.4.

In Figure 8 we plot the $M_* - \sigma$ distribution of the 37¹² confirmed UCMGs (squared symbols).

For comparison, we overplot a sample of normal-sized ETGs (red small dots) analyzed in Tortora et al. (2018) and derived from SDSS-III/BOSS (Baryon Oscillation Spectroscopic Survey) Data Release 10¹³ (DR10, Ahn et al. 2014). We restrict the BOSS sample to the redshift

¹² We have in total 19 confirmed systems from the three new spectroscopic runs and 18 from the runs presented in T18 and confirmed on the basis of the new mass-calculation set-up.

¹³ The data catalogs are available from http://www.sdss3.org/dr10/spectro/galaxy_portsmouth.php.

range $0.15 \lesssim z \lesssim 0.5$, to provide a direct comparison with the sample of UCMGs. For these systems, in [Tortora et al. \(2018\)](#) we have derived stellar masses using the same set-up adopted in this paper, while the velocity dispersion values are originally measured in a circular aperture of radius 1 arcsec.

The distribution of all the confirmed UCMGs presents a large scatter, which is mainly the consequence of the large errors on the velocity dispersion values (see typical error bars on top right corner of the figure). We plot with full squares UCMGs classified in the high-quality group and open squares the ones belonging to the low quality group, according to the definition given in [Section 3.4](#).

Finally, in order to highlight significant patterns in this figure, we also plot the running mean and 1σ scatter for the UCMGs and BOSS galaxies. The running means obtained from the UCMGs in the HQ subsample (i.e. the grey shaded region in the figure) and that obtained for all the normal-sized BOSS galaxies (i.e. red region) differ significantly. The UCMGs have systematically larger velocity dispersions at any fixed mass, especially above $\log M_*/M_\odot = 11.05$, and this result is consistent with other studies of high- z systems ([vanDokkum et al. 2009](#); [Toft et al. 2012](#)) and local massive relics ([Ferré-Mateu et al. 2017](#)). The offset almost disappears when including the LQ UCMGs, which, at least for larger masses, are scattered toward lower σ and are consistent with the normal ETG distribution within the (large) errors.

We consider the offset between BOSS and HQ UCMGs robust and statistically significant, although we anticipate that with better data we will be able to improve the measurement errors and also increase the size of the sample. Nevertheless, taking these findings at face value, one can speculate about possible explanations for this offset. The first possibility is that more compact massive galaxies host a more massive black hole (e.g. [van den Bosch et al. 2012, 2015](#); [Ferré-Mateu et al. 2017](#)) which might influence the kinematics in the innermost region. Another possibility is that the IMF in very massive galaxies can be different from an universal Milky Way-like IMF. However, whereas for larger galaxies the bottom-heavy IMF is restricted only in the very central region ($\sim 0.2 - 0.3R_e$), for relics the IMF is heavier than Salpeter everywhere up to few effective radii. One physical scenario able to explain this difference would be that only the “in situ” stars formed during the first phase of the assembly of massive ETGs form with a dwarf-rich IMF, while accreted stars (only present in normal-sized ETGs) form with a standard IMF ([Chabrier et al. 2014](#)).

We will investigate these possibilities in a dedicated paper, already in preparation. There, we will compare

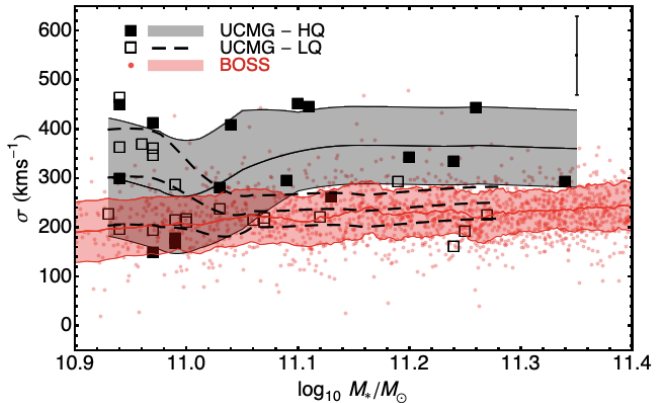


Figure 8. Distribution on the $M_* - \sigma$ plane for the 37 confirmed UCMGs compared with a sample of elliptical galaxies (red symbols) from the BOSS survey. Filled squared symbols are UCMGs classified as high quality (HQ), with spectra that satisfy at the same time the three conditions $SR \geq 0.3$, $S/N_{spec} \geq 3.5$ and $(S/N)_{O-K} \geq 6.5$. Empty squares are instead classified as low-quality (LQ) since their spectra do not satisfy one or more of the aforementioned criteria. For each sample, running means and 1σ scatter are overplotted. In the top-right corner we show the mean error bar for the UCMG velocity dispersions. For both UCMGs and the sample of ellipticals, velocity dispersions are calculated within 1 effective radius, as explained in the text.

these (and new) measurements with theoretically motivated predictions, including more than one galaxy formation recipe. We will check whether the $M_* - \sigma$ relation preserves the footprints of the stellar and dark assembly of these systems, trying to quantify the dynamical contribution of a central supermassive black hole and a bottom-heavy IMF.

In conclusion, given the large uncertainties on the velocity dispersion measurements and the fact that we cannot yet distinguish between relics and non-relics, we provide here only some preliminary speculative explanations. In the future, we aim at consolidating this result with a larger number of systems, to increase the statistics, and using spectroscopic data of better quality, in order to have more robust velocity dispersion estimates. With new, better spectroscopic data we will also be able to constrain the age of the systems, which is the crucial ingredient to identify relics among the confirmed UCMGs.

5. CONCLUSIONS

The existence of ultra-compact massive galaxies (UCMGs) at $z < 1$ and their evolution up to the local Universe challenges the currently accepted galaxy formation models. In the effort of “bridging the gap” between the high redshift red nuggets and the local relics, we have started a census of UCMGs at intermediate redshifts. In particular, in the first paper of this

series (Tortora et al. 2016), we have demonstrated that the high image quality, the large area covered, the excellent spatial resolution and the exquisite seeing of the Kilo Degree Survey (KiDS) make this survey perfect to find UCMGs candidates. In the second paper (Tortora et al. 2018b) we have started a multi-site and multi-telescope spectroscopic observational campaign to confirm as many candidates as possible with the final goal of building the largest spectroscopically confirmed sample of UCMGs in the redshift range $0.15 \lesssim z \lesssim 0.5$.

In this third paper of the series, we have continued in this direction and we have:

- spectroscopically followed up a sample of 33 UCMG candidates at redshifts $0.15 \lesssim z \lesssim 0.5$, found in 333 deg^2 of KiDS. We have provided details on how the galaxies have been photometrically selected and discussed the spectroscopic campaign on the INT and TNG telescopes, including also the main data reduction steps for each instrument;
- obtained the spectroscopic redshift and velocity dispersion values for these objects and for the 28 objects already presented in T18. To this purpose, we have used the Optimised Modelling of Early-type Galaxy Aperture Kinematics pipeline (OMEGA-K, D’Ago et al., in prep.);
- confirmed 19 out of 33 as UCMGs, with the newly spectroscopically based masses and effective radii. This translates into a success rate of 58%, in good agreement with the one reported in T18. In addition, using the new mass set-up we have confirmed 18 out of 27 UCMGs from T18, corresponding to a success rate of 67%. One galaxy from T18 did not qualify as UCMG candidate when re-computing its mass with the newly defined set-up. Thus, in total, we confirm as UCMGs 37 out of 61 candidates, implying a success rate of 60%. Allowing a tolerance at the 1σ -level (3σ -level) on the effective radii and stellar masses inferred from the spectroscopic redshifts, we confirm as UCMGs 57 (61) out of 61 UCMG candidates with a success rate of $\sim 93\%$ (100%);
- quantified the effect of contamination and incompleteness due to the difference in redshift between the photometric and spectroscopic values. We have found that the true number counts for UCMGs at $z < 0.5$ is ~ 15 per cent higher than the values found in a photometrically selected sample;
- obtained the UCMG number counts, after correcting them with the incompleteness and the contamination factors, and their evolution with redshift in

the range $0.15 < z < 0.5$. We have also compared our new results with these obtained in T18, using a different set-up for the mass inference and in the literature. We have confirmed the clear decrease of the number counts with the cosmic time already found in T18, from $\sim 9 \times 10^{-6} \text{ Mpc}^{-3}$ at $z \sim 0.5$, to $\sim 10^{-6} \text{ Mpc}^{-3}$ at $z \sim 0.15$, ~ 9 times less in about 3 Gyr;

- shown the distribution of the 37 confirmed UCMGs in the $M_* - \sigma$ plane. We have corrected the sigma values to a common aperture of one effective radius in order to compare the UCMGs distribution with that of a sample of normal-sized ellipticals from the BOSS Survey. Despite the large uncertainties on the velocity dispersion measurements, due to the low signal-to-noise of the spectra, we found tentative evidence suggesting that the UCMGs have larger values compared to regular ETGs of same mass. This seems to be statistically significant at least for the high-quality sample and large masses. This preliminary result, in agreement with what expected from the evolution of massive and compact galaxies, will be checked again once new, higher resolution spectroscopy (already awarded) will be obtained.

After KiDS will be completed, we expect to at least double the number of confirmed UCMGs, and thus reduce by a factor $\sim 40\%$ the uncertainties on the number counts, while keeping the systematics under full control.

In the future, we also plan to continue to enlarge the sample of spectroscopically confirmed UCMGs at low and intermediate redshifts, based on photometric candidates from the KiDS survey. Moreover, thanks to already awarded spectroscopic data with much higher S/N, which will allow us to perform a detailed stellar population analysis, we will separate relics from younger UCMGs. With the higher signal-to-noise spectra that we will soon have at our disposal, we aim at unambiguously demonstrate that the majority the objects in our sample are indeed red and dead, as already indicated by their photometric colors and that they have formed their baryonic matter early on in cosmic time, with a fast and “bursty” star formation episode. In this way, we will be able to unambiguously confirm the two-phase formation scenario proposed for the mass assembly of massive/giant ETGs (Oser et al. 2010).

Relics, UCMGs as old as the Universe, are the only systems that, with current observing facilities, allow us to study the physical processes that shaped the mass assembly of massive galaxies in the high- z universe with

the amount of details currently reachable only for the near-by Universe.

ACKNOWLEDGEMENTS

DS is a member of the International Max Planck Research School (IMPRS) for Astronomy and Astrophysics at the Universities of Bonn and Cologne. CT acknowledges funding from the INAF PRIN-SKA 2017 program 1.05.01.88.04. MS acknowledges financial support from the VST project (PI: P. Schipani). CS has received funding from the European Union's Horizon 2020 research and innovation programme under the Marie Skłodowska-Curie actions grant agreement No 664931. GD acknowledges support from CONICYT project Basal AFB-170002. MB acknowledges the *INAF PRIN-SKA 2017 program 1.05.01.88.04*, the funding from *MIUR Premiale 2016: MITIC* and the financial contribution from the agreement ASI/INAF nr. 2018-23-HH.0 *Euclid mission scientific activities - Phase D*. The INT is operated on the island of La Palma by the Isaac Newton Group of

Telescopes in the Spanish Observatorio del Roque de los Muchachos of the Instituto de Astrofísica de Canarias. Based on observations made with the Italian Telescopio Nazionale Galileo (TNG) and Isaac Newton (INT) telescopes operated by the Fundación Galileo Galilei of the INAF (Istituto Nazionale di Astrofisica) and the Isaac Newton Group of Telescopes, both of them installed in the Spanish Observatorio del Roque de los Muchachos of the Instituto de Astrofísica de Canarias. Based on data products from observations made with ESO Telescopes at the La Silla Paranal Observatory under programme IDs 177.A-3016, 177.A-3017 and 177.A-3018, and on data products produced by Target/OmegaCEN, INAF-OACN, INAF-OAPD and the KiDS production team, on behalf of the KiDS consortium. OmegaCEN and the KiDS production team acknowledge support by NOVA and NWO-M grants. Members of INAF-OAPD and INAF-OACN also acknowledge the support from the Department of Physics & Astronomy of the University of Padova, and of the Department of Physics of Univ. Federico II (Naples).

REFERENCES

- Ahn C. P., Alexandroff, R., Allende Prieto, C., et al., 2012, *ApJS*, 203, 21
- Ahn C. P., Alexandroff, R., Allende Prieto, C., et al., 2014, *ApJS*, 211, 17
- Arnouts S., Cristiani S., Moscardini L., et al., 1999, *MNRAS*, 310, 540
- Beasley M. A., Trujillo I., Leaman R., Montes M., 2018, *Nature*, 555, 483
- Bertin E. & Arnouts S., 1996, *A&AS*, 117, 393
- Blake, C., Amon, A., Childress, M., et al., 2016, *MNRAS*, 462, 4240
- Brescia M., Cavuoti S., D'Abrusco R., Longo G., & Mercurio A., 2013, *ApJ*, 772, 140
- Brescia M., Cavuoti S., Longo G., De Stefano V., 2014, *A&A*, 568, A126
- Bruzual G. & Charlot S., 2003, *MNRAS*, 344, 1000
- Buitrago, F., Ferreras, I., Kelvin, L. S., et al., 2018, *ArXiv e-prints*
- Capaccioli M. & Schipani P., 2011, *The Messenger*, 146, 2
- Cappellari, M., Bacon, R., Bureau, M., et al., 2006, *MNRAS*, 366, 1126-1150
- Cappellari, M., McDermid, R. M., Alatalo, K., et al., 2012, *Nature*, 484 485-488
- Cappellari M., 2017, *MNRAS*, 466, 798
- Cavuoti S., Brescia M., De Stefano V., Longo G., 2015a, *Experimental Astronomy*, 39, 45
- Cavuoti, S., Brescia, M., Tortora, C., et al., 2015b, *MNRAS*, 452, 3100
- Cavuoti, S., Tortora, C., Brescia, M., et al., 2017, *MNRAS*, 466, 2039
- Chabrier G., 2001, *ApJ*, 554, 1274
- Chabrier, G., Hennebelle, P. & Charlot, S., 2014, *ApJ*, 2, 75
- Charbonnier, A., Huertas-Company, M., Gonçalves, T. S., et al., 2017, *MNRAS*, 469, 4523
- Conroy, C. & van Dokkum, P., 2012, *ApJ*, 747, 69
- D'Ago, Giuseppe, Napolitano, R. N., Tortora, C., Spiniello, Chiara & La Barbera, Francesco, 2018, *VST in the Era of the Large Sky Surveys*, 15
- Daddi, E., Renzini, A., Pirzkal, N., et al., 2005, *ApJ*, 626, 680
- Damjanov, I., Abraham, R. G., McCarthy P. J., Glazebrook, K., 2009, *Bulletin of the American Astronomical Society*, 41, 512
- Damjanov I., Abraham R., Glazebrook K. et al., 2011, *ApJL*, 739, L44
- Damjanov I., Geller M. J., Zahid H. J., Hwang H. S., 2015a, *ApJ*, 806, 158
- Damjanov I., Hwang H. S., Geller M. J., Chilingarian I., 2014, *ApJ*, 793, 39
- Damjanov I., Zahid H. J., Geller M. J., Hwang H. S., 2015b, *ArXiv e-prints*
- Dawson K. S. et al., 2013, *AJ*, 145, 10

- de Jong, J. T. A., Verdoes Kleijn, G. A., Boxhoorn, D. R., et al., 2015, *A&A*, 582, A62
- de Jong, J. T. A., Kleijn, G. A. Erben, T., et al., 2017, *A&A*, 604, A134
- Dekel A., Burkert A., 2014, *MNRAS*, 438, 1870
- Driver, S. P., Hill, D. T. Kelvin, L. S., et al., 2011, *MNRAS*, 413, 971
- Edge A., Sutherland W., The Viking Team, 2014, *VizieR Online Data Catalog*, 2329, 0
- Faber, S. M. & Jackson, R. E., 1976, *ApJ*, 204, 668-683
- Fasano, G., Marmo, C. and Varela, J., et al., 2006, *A&A*, 445, 805-871
- Ferré-Mateu A., Vazdekis A., Trujillo I., Sánchez-Blázquez P., Ricciardelli E., de la Rosa I. G., 2012, *MNRAS*, 423, 632
- Ferré-Mateu A., Mezcua M., Trujillo I., Balcells M., van den Bosch R. C. E., 2015, *ApJ*, 808, 79
- Ferré-Mateu A., Trujillo I., Martín-Navarro I., Vazdekis A., Mezcua M., Balcells M., Domínguez L., 2017, *MNRAS*, 467, 1929
- Gargiulo, A., Bolzonella, M., Scodreggio, M., et al., 2016a, *ArXiv e-prints*
- Guo, Q., White, S., Boylan-Kolchin, M., et al., 2011, *MNRAS*, 413, 101
- Guo Q., White S., Angulo R. E., Henriques B., Lemson G., Boylan-Kolchin M., Thomas P., Short C., 2013, *MNRAS*, 428, 1351
- Hyde, J. B. & Bernardi, M., 2009, *MNRAS*, 394, 1978-1990
- Hopkins P. F., Hernquist L., Cox T. J., Keres D., Wuyts S., 2009, *ApJ*, 691, 1424
- Hopkins, A. M., Driver, S. P., Brough, S., et al., 2013, *MNRAS*, 430, 2047-2066
- Hsu L.-Y., Stockton A., Shih H.-Y., 2014, *ApJ*, 796, 92
- Ilbert, O., Arnouts, S., McCracken, H. J., et al., 2006, *A&A*, 457, 841
- Komatsu, E., Smith, K. M., Dunkley, J., et al., 2011, *ApJS*, 192, 18
- La Barbera F., de Carvalho R. R., Kohl-Moreira J. L., Gal R. R., Soares-Santos M., Capaccioli M., Santos R., Sant'anna N., 2008, *PASP*, 120, 681
- La Barbera F., de Carvalho R. R., de La Rosa I. G., Lopes P. A. A., Kohl-Moreira J. L., Capelato H. V., 2010, *MNRAS*, 408, 1313
- La Barbera F., Ferreras I., Vazdekis A., de la Rosa I. G., de Carvalho R. R., Trevisan M., Falcón-Barroso J., Ricciardelli E., 2013, *MNRAS*, 433, 3017
- Läsker R., van den Bosch R. C. E., van de Ven G., et al., 2013, *MNRAS*, 434, L31
- Maraston, C., Pforr, J., Henriques, B. M., et al., 2013, *MNRAS*, 435, 2764
- Martín-Navarro I., La Barbera F., Vazdekis A., et al., 2015, *MNRAS*, 451, 1081
- Oser L., Ostriker J. P., Naab T., Johansson, P. H., Burkert, A., 2010, *ApJ*, 725, 2312
- Poggianti, B. M., Moretti, A., Calvi, R. et al., 2013a, *ApJ*, 77, 125
- Poggianti, B. M., Calvi, R., Bindoni, et al., 2013c, *ApJ*, 762, 77
- Quilis, V. & Trujillo, I., 2013, *ApJL*, 773, L8
- Roy, N., Napolitano, N. R., La Barbera, F., et al., 2018, *MNRAS*, 80, 1
- Saulder C., van den Bosch R. C. E., Mieske S., 2015, *A&A*, 578, A134
- Schlafly E. F., Finkbeiner D. P., 2011, *ApJ*, 737, 103
- Shih H.-Y., Stockton A., 2011, *ApJ*, 733, 45
- Spiniello, C., Trager, S. C., Koopmans, L. V. E. & Chen, Y. P., 2012, *ApJL*, 753, L32
- Spiniello, C., Trager, S., Koopmans, L. V. E. & Conroy, C., 2014, *MNRAS*, 438, 1483-1499
- Spiniello, C., Barnabè, M., Koopmans, L. V. E. & Trager, S. C., 2015, *MNRAS*, 452, L21-L25
- Stockton A., Shih H.-Y., Larson K., Mann A. W., 2014, *ApJ*, 780, 134
- Stringer M., Trujillo I., Dalla Vecchia C., Martinez-Valpuesta I., 2015, *MNRAS*, 449, 2396
- Taylor E. N., Franx M., Glazebrook K., Brinchmann J., van der Wel A., van Dokkum P. G., 2010, *ApJ*, 720, 723
- Thomas D., Maraston C., Bender R., Mendes de Oliveira C., 2005, *ApJ*, 621, 673
- Toft, S., Gallazzi, A., Zirm, A. et al., 2012, *ApJ*, 754, 3
- Tortora C., Romanowsky A. J., Napolitano N. R., 2013, *ApJ*, 765, 8
- Tortora C., Napolitano N. R., Saglia R. P., et al., 2014, *MNRAS*, 445, 162
- Tortora, C., Napolitano, N. R., La Barbera, F., et al., 2016, *MNRAS*, 457, 2845
- Tortora, C., Napolitano, N. R., Roy, N., et al., 2018a, *MNRAS*, 473, 969
- Tortora, C., Napolitano, N. R., Spavone, M., 2018b, *MNRAS*, 481, 4728-4752
- Trenti M. & Stiavelli M., 2008, *ApJ*, 676, 767
- Trujillo, I., Förster Schreiber, N. M., Rudnick, G., et al., 2006, *ApJ*, 650, 18
- Trujillo I., Cenarro A. J., de Lorenzo-Cáceres A., et al., 2009, *ApJL*, 692, L118
- Trujillo I., Ferré-Mateu A., Balcells M., Vazdekis A., Sánchez-Blázquez P., 2014, *ApJL*, 780, L20
- Valentinuzzi, T., Fritz, J., Poggianti, B. M., et al., 2010, *ApJ*, 712, 226

- van den Bosch, R. C. E., Gebhardt, K., Gültekin, K. et al., 2012, *Nature*, 491, 729–731
- van den Bosch, R. C. E., Gebhardt, K., Gültekin
- van Dokkum, P. G., Kriek, M. & Franx, M., 2009, *Nature*, 460, 717
- van Dokkum, P. G., Whitaker, K. E., Brammer, G., et al., 2010, *ApJ*, 709, 1018
- Vazdekis A., Sánchez-Blázquez P., Falcón-Barroso J., et al., 2010, *MNRAS*, 404, 1639
- Wellons, S., Torrey, P., Ma, C. P., et al., 2015, *MNRAS*, 449, 361-372
- Wellons, S., Torrey, P., Ma, C. P., et al., 2016, *MNRAS*, 456, 1030
- Werner N., Lakhchaura K., Canning R. E. A., Gaspari M., & Simionescu A., 2018, *MNRAS*, 477, 3886-3891
- Wright, A. H., Hildebrandt, H., Kuijken, K., et al., 2018, *arXiv e-prints*, 1812.06077
- Yıldırım A., van den Bosch R. C. E., van de Ven G., et al., 2015, *MNRAS*, 452, 1792

APPENDIX

In order to quantify the impact of the systematics on the UCMG selection, we have created, in Section 4.2 the UCMG_SPEC sample: a sample of 55 UCMGs with spectroscopic redshifts from the literature, similar to the sample used in T18 but selected with the new mass set-up. We have gathered these spectroscopic redshifts from SDSS (Ahn et al. 2012, 2014), GAMA (Driver et al. 2011), which overlap the KiDS fields in the Northern cap, and 2dFLenS (Blake et al. 2016), observed in the Southern hemisphere. Here in this Appendix we provide the basic photometric and structural parameters for such 55 UCMGs in the spectroscopically selected sample. In particular, in Table 7 we show r -band Kron magnitude, aperture magnitudes used in the SED fitting, spectroscopic redshifts and stellar masses (in decimal logarithm). Sérsic structural parameters from the 2DPHOT fit of g -, r -, and i -band KiDS surface photometry, as such as χ^2 s and S/N values, are instead presented in Table 8.

Table 7. Integrated photometry for the 55 systems in the UCMG_SPEC sample. From left we show: a) progressive ID number; b) KIDS identification name; c) r -band KiDS MAG_AUTO; d-g) u -, g -, r - and i -band KiDS magnitudes measured in an aperture of 6 arcsec of diameter with 1σ errors; h) spectroscopic redshift. All the magnitudes have been corrected for Galactic extinction using Schlafly & Finkbeiner (2011) maps.

ID	name	MAG_AUTO_r	$u_{6''}$	$g_{6''}$	$r_{6''}$	$i_{6''}$	z_{phot}	$\log_{10} M_*/M_{\odot}$
L1	KIDS J025942.84-315933.74	18.96	22.61 ± 0.13	20.39 ± 0.008	18.97 ± 0.003	18.52 ± 0.007	0.29	11.00
L2	KIDS J032700.87-300112.34	20.37	23.02 ± 0.21	21.93 ± 0.04	20.34 ± 0.009	19.43 ± 0.01	0.33	11.00
L3	KIDS J084320.59-000543.77	18.52	21.55 ± 0.06	19.71 ± 0.005	18.53 ± 0.002	18.12 ± 0.005	0.24	10.93
L4	KIDS J084738.70+011220.57	18.41	21.78 ± 0.12	19.70 ± 0.006	18.44 ± 0.002	18.02 ± 0.005	0.18	11.00
L5	KIDS J085335.58+001805.97	18.84	21.67 ± 0.09	20.13 ± 0.009	18.95 ± 0.003	18.63 ± 0.008	0.33	10.94
L6	KIDS J085344.88+024948.47	18.49	21.63 ± 0.07	19.70 ± 0.005	18.50 ± 0.002	18.08 ± 0.005	0.23	10.93
L7	KIDS J090324.20+022645.50	17.25	20.24 ± 0.02	18.34 ± 0.002	17.34 ± 0.001	16.98 ± 0.001	0.19	11.21
L8	KIDS J090935.74+014716.81	18.68	22.52 ± 0.17	20.15 ± 0.008	18.75 ± 0.002	18.23 ± 0.006	0.22	11.02
L9	KIDS J092055.70+021245.66	18.87	22.80 ± 0.21	20.37 ± 0.01	18.89 ± 0.003	18.46 ± 0.005	0.28	11.01
L10	KIDS J102653.56+003329.15	17.39	20.49 ± 0.02	18.52 ± 0.002	17.45 ± 0.001	17.04 ± 0.002	0.17	11.17
L11	KIDS J112825.16-015303.29	20.94	23.90 ± 0.57	22.56 ± 0.06	20.91 ± 0.01	20.19 ± 0.04	0.46	10.94
L12	KIDS J113612.68+010316.86	19.01	22.07 ± 0.08	20.26 ± 0.007	19.02 ± 0.003	18.59 ± 0.005	0.22	10.97
L13	KIDS J114248.56+001215.63	17.02	19.72 ± 0.01	17.95 ± 0.002	17.14 ± 0.0008	16.71 ± 0.001	0.11	10.58
L14	KIDS J115652.47-002340.77	18.83	21.98 ± 0.09	20.06 ± 0.007	18.83 ± 0.003	18.08 ± 0.006	0.26	11.14
L15	KIDS J120251.61+013825.15	17.89	20.69 ± 0.03	19.39 ± 0.003	18.04 ± 0.001	17.75 ± 0.003	0.20	11.04
L16	KIDS J120818.93+004600.16	17.74	20.65 ± 0.03	18.88 ± 0.004	17.93 ± 0.001	17.56 ± 0.002	0.18	10.92
L17	KIDS J120902.53-010503.08	18.83	22.68 ± 0.21	20.16 ± 0.008	18.82 ± 0.003	18.36 ± 0.008	0.27	11.04
L18	KIDS J121152.97-014439.23	18.60	21.64 ± 0.08	19.79 ± 0.006	18.65 ± 0.003	18.23 ± 0.005	0.23	10.96
L19	KIDS J121555.27+022828.13	20.56	23.36 ± 0.32	22.21 ± 0.04	20.53 ± 0.01	19.81 ± 0.02	0.47	10.97
L20	KIDS J140620.09+010643.00	19.16	22.55 ± 0.13	20.68 ± 0.01	19.19 ± 0.004	18.70 ± 0.009	0.37	11.28
L21	KIDS J141108.94-003647.51	19.22	22.27 ± 0.14	20.57 ± 0.01	19.20 ± 0.004	18.74 ± 0.01	0.29	10.98
L22	KIDS J141200.92-002038.65	19.19	22.94 ± 0.27	20.76 ± 0.02	19.21 ± 0.005	18.69 ± 0.02	0.28	11.08
L23	KIDS J141213.62+021202.06	18.37	19.30 ± 0.01	19.14 ± 0.004	18.38 ± 0.002	18.16 ± 0.005	0.30	11.06
L24	KIDS J141415.53+000451.51	18.99	22.86 ± 0.17	20.41 ± 0.009	19.00 ± 0.003	18.50 ± 0.006	0.30	11.07
L25	KIDS J141417.33+002910.20	18.77	21.73 ± 0.07	20.04 ± 0.007	18.77 ± 0.003	18.34 ± 0.006	0.30	11.03
L26	KIDS J141728.44+010626.61	17.90	20.94 ± 0.04	19.06 ± 0.004	17.98 ± 0.002	17.59 ± 0.003	0.18	10.96
L27	KIDS J141828.24-013436.27	18.82	21.13 ± 0.07	19.90 ± 0.006	18.80 ± 0.003	18.39 ± 0.005	0.43	11.26
L28	KIDS J142033.15+012650.38	19.38	23.58 ± 0.38	20.79 ± 0.02	19.37 ± 0.005	18.89 ± 0.01	0.32	10.92
L29	KIDS J142041.17-003511.27	18.95	22.40 ± 0.14	20.37 ± 0.009	19.01 ± 0.003	18.51 ± 0.005	0.25	11.00
L30	KIDS J142235.50-014207.95	19.24	23.10 ± 0.27	20.65 ± 0.01	19.27 ± 0.004	18.82 ± 0.009	0.28	10.92

Table 7. – continued from previous page

ID	name	MAG_AUTO_r	u_6''	g_6''	r_6''	i_6''	z_{phot}	$\log_{10} M_*/M_{\odot}$
L31	KIDS J142606.67+015719.28	19.33	22.97 ± 0.22	20.69 ± 0.01	19.30 ± 0.005	18.86 ± 0.01	0.35	11.14
L32	KIDS J142800.20-001026.87	18.75	19.42 ± 0.01	19.33 ± 0.004	18.83 ± 0.003	18.56 ± 0.009	0.33	11.05
L33	KIDS J142922.11+011450.00	18.69	21.95 ± 0.12	20.09 ± 0.008	18.69 ± 0.003	18.35 ± 0.007	0.37	11.10
L34	KIDS J143025.44-023311.23	18.80	19.25 ± 0.01	19.13 ± 0.005	18.79 ± 0.003	18.49 ± 0.007	0.40	11.15
L35	KIDS J143155.56-000358.65	19.34	22.74 ± 0.18	20.73 ± 0.02	19.32 ± 0.004	18.82 ± 0.007	0.34	11.04
L36	KIDS J143419.53-005231.62	19.14	22.64 ± 0.17	20.79 ± 0.01	19.13 ± 0.004	18.57 ± 0.005	0.46	11.20
L37	KIDS J143459.11-010154.63	19.37	22.95 ± 0.25	20.70 ± 0.01	19.36 ± 0.004	18.88 ± 0.01	0.28	10.96
L38	KIDS J143528.88+013055.39	19.31	22.82 ± 0.33	20.65 ± 0.02	19.31 ± 0.004	18.81 ± 0.01	0.28	10.91
L39	KIDS J143607.24+003902.15	19.18	22.87 ± 0.23	20.64 ± 0.01	19.17 ± 0.004	18.72 ± 0.008	0.30	10.92
L40	KIDS J143611.55+000718.29	18.27	21.53 ± 0.06	19.57 ± 0.004	18.29 ± 0.002	17.87 ± 0.004	0.22	11.06
L41	KIDS J143616.24+004801.40	19.24	22.78 ± 0.25	20.62 ± 0.01	19.24 ± 0.004	18.76 ± 0.009	0.29	11.08
L42	KIDS J143805.25-012729.78	19.29	22.74 ± 0.19	20.64 ± 0.01	19.29 ± 0.004	18.73 ± 0.007	0.29	10.94
L43	KIDS J144138.27-011840.93	19.35	23.62 ± 0.48	20.78 ± 0.01	19.35 ± 0.004	18.83 ± 0.008	0.29	11.00
L44	KIDS J144557.12-013510.24	19.16	22.12 ± 0.13	20.45 ± 0.009	19.15 ± 0.004	18.73 ± 0.009	0.29	10.92
L45	KIDS J144751.78-014927.41	18.61	21.88 ± 0.11	19.87 ± 0.007	18.63 ± 0.003	18.17 ± 0.005	0.21	10.93
L46	KIDS J144924.11-013845.59	19.40	22.79 ± 0.24	20.82 ± 0.02	19.39 ± 0.005	18.89 ± 0.009	0.27	11.01
L47	KIDS J145245.48+025321.32	17.69	20.60 ± 0.03	18.74 ± 0.002	17.77 ± 0.001	17.50 ± 0.003	0.26	11.18
L48	KIDS J145356.13+001849.32	20.32	23.24 ± 0.30	22.06 ± 0.04	20.32 ± 0.009	19.68 ± 0.03	0.42	11.16
L49	KIDS J145638.63+010933.24	19.66	23.21 ± 0.26	21.31 ± 0.02	19.63 ± 0.006	19.09 ± 0.01	0.42	11.18
L50	KIDS J153936.50-003904.58	20.15	21.46 ± 0.09	20.76 ± 0.02	20.11 ± 0.01	19.70 ± 0.02	0.47	10.99
L51	KIDS J154949.48-003655.52	19.02	19.38 ± 0.01	19.19 ± 0.004	19.02 ± 0.004	18.86 ± 0.01	0.47	11.30
L52	KIDS J155133.16+005709.77	19.37	24.82 ± 1.76	20.95 ± 0.02	19.34 ± 0.005	18.86 ± 0.01	0.42	11.29
L53	KIDS J220453.48-311200.94	19.32	22.90 ± 0.23	20.84 ± 0.01	19.34 ± 0.004	18.87 ± 0.005	0.26	10.96
L54	KIDS J231410.93-324101.31	19.26	22.59 ± 0.16	20.56 ± 0.009	19.26 ± 0.004	18.75 ± 0.006	0.29	11.01
L55	KIDS J233148.39-333402.05	20.46	24.47 ± 0.74	22.12 ± 0.04	20.44 ± 0.009	19.78 ± 0.02	0.48	11.09

Table 8. Structural parameters derived running 2DPHOT on g -, r - and i -bands for the 55 in the UCMG_SPEC sample. For each band we show: a) circularized effective radius Θ_e , measured in arcsec, b) circularized effective radius R_e , measured in kpc (calculated using z_{phot} values listed in Table 1), c) Sérsic index n , d) axis ratio q , e) χ^2 of the surface photometry fit, f) χ'^2 of the surface photometry fit including only central pixels and g) the signal-to-noise ratio S/N of the photometric images, defined as the inverse of the error on MAG_AUTO.

ID	g -band							r -band							i -band						
	Θ_e	R_e	n	q	χ^2	χ'^2	S/N	Θ_e	R_e	n	q	χ^2	χ'^2	S/N	Θ_e	R_e	n	q	χ^2	χ'^2	S/N
L1	0.25	1.07	4.11	0.34	1.02	1.05	123	0.27	1.19	4.54	0.37	1.07	1.35	367	0.29	1.27	5.62	0.39	1.00	0.93	147
L2	0.05	0.24	4.66	0.12	1.01	0.98	32	0.16	0.74	4.03	0.33	1.02	1.01	127	0.24	1.12	2.96	0.42	0.98	0.87	96
L3	0.29	1.12	4.40	0.58	1.03	1.06	190	0.26	1.01	5.59	0.61	1.20	1.72	506	0.33	1.25	8.48	0.68	1.01	0.95	203
L4	0.46	1.36	3.06	0.27	1.01	1.04	165	0.46	1.39	4.38	0.25	1.07	1.42	462	0.45	1.35	3.33	0.27	1.01	0.96	177
L5	0.56	2.65	10.56	0.75	1.02	0.99	94	0.23	1.09	9.84	0.80	1.12	1.87	279	0.22	1.03	9.27	0.73	1.02	1.04	99
L6	0.39	1.44	3.83	0.46	1.02	1.03	185	0.34	1.25	4.13	0.44	1.08	1.47	443	0.34	1.26	4.00	0.42	1.05	1.10	190
L7	0.46	1.45	4.34	0.24	1.05	1.40	492	0.23	0.73	7.04	0.29	1.34	2.89	1003	0.54	1.70	4.82	0.26	1.06	1.32	641
L8	0.56	1.96	9.95	0.81	0.83	0.86	110	0.14	0.48	10.07	0.76	1.13	1.84	357	0.30	1.05	9.97	0.77	1.01	1.00	152
L9	0.41	1.76	1.97	0.34	1.03	1.13	95	0.34	1.46	1.99	0.32	1.04	1.34	351	0.28	1.20	3.02	0.30	1.00	1.04	206
L10	0.43	1.26	2.70	0.29	1.07	11.51	360	0.32	0.95	3.64	0.29	1.12	25.78	1092	0.34	1.01	3.18	0.29	1.03	9.58	464
L11	0.31	1.78	8.80	0.21	0.99	1.10	16	0.25	1.46	8.54	0.44	1.03	0.99	74	0.21	1.22	3.66	0.59	1.01	1.28	32
L12	0.29	1.02	4.03	0.26	1.07	1.03	130	0.14	0.48	7.96	0.27	1.05	1.20	327	0.11	0.40	8.07	0.25	1.02	0.96	188
L13	0.37	1.39	4.79	0.38	1.03	0.99	602	0.20	1.26	6.53	0.40	1.03	1.18	1109	0.26	1.39	8.63	0.38	1.01	0.94	618
L14	0.71	1.47	3.60	0.22	1.12	1.46	140	0.64	0.79	5.26	0.23	1.40	2.32	381	0.70	1.03	3.48	0.24	1.04	1.19	163
L15	0.28	0.93	9.55	0.72	1.08	1.54	275	0.35	1.15	7.85	0.64	1.31	3.19	621	0.45	1.50	10.06	0.73	1.04	1.13	239
L16	0.50	1.49	7.65	0.38	1.02	7.99	210	0.45	1.34	7.52	0.41	1.10	23.21	673	0.72	2.14	7.51	0.45	1.04	11.05	357
L17	0.36	1.49	2.64	0.30	1.01	0.91	127	0.35	1.47	2.88	0.28	1.12	1.51	410	0.35	1.46	2.42	0.27	1.01	0.94	128
L18	0.52	1.94	8.65	0.52	1.04	1.14	154	0.38	1.42	7.59	0.61	1.03	1.35	363	0.25	0.93	8.95	0.59	1.04	1.04	193
L19	0.17	1.01	0.69	0.14	0.98	0.95	29	0.20	1.19	3.60	0.51	0.98	0.98	97	0.17	1.04	4.96	0.49	1.00	1.01	69
L20	0.32	1.64	6.76	0.29	1.02	1.21	85	0.26	1.36	7.52	0.33	1.07	1.56	276	0.25	1.27	9.23	0.35	1.02	1.25	115
L21	0.40	1.76	2.80	0.56	1.04	1.07	76	0.30	1.32	3.13	0.45	1.01	1.09	261	0.25	1.10	4.71	0.40	0.99	0.86	75
L22	0.34	1.44	5.00	0.33	0.99	0.93	52	0.32	1.35	6.30	0.39	1.01	1.02	217	0.33	1.41	6.13	0.42	1.02	0.99	66
L23	0.18	0.81	7.66	0.61	1.06	1.24	265	0.28	1.21	7.51	0.58	1.28	2.27	507	0.76	3.33	3.62	0.60	1.05	1.17	175
L24	0.38	1.69	3.99	0.46	1.02	1.01	108	0.31	1.40	4.26	0.42	1.04	1.21	316	0.30	1.33	5.03	0.42	0.99	0.89	169
L25	0.31	1.36	5.12	0.81	1.02	0.97	142	0.32	1.41	4.72	0.85	1.04	1.22	383	0.27	1.18	7.84	0.88	1.02	0.96	173
L26	0.54	1.63	3.35	0.35	1.03	1.08	244	0.48	1.47	3.92	0.31	1.07	1.53	555	0.45	1.36	4.74	0.33	1.03	1.08	294
L27	0.22	1.22	3.66	0.52	1.02	1.83	168	0.23	1.30	3.95	0.58	1.02	6.89	399	0.24	1.36	3.15	0.56	1.05	2.85	232
L28	0.19	0.90	3.87	0.15	1.02	0.89	72	0.22	1.02	4.04	0.17	1.01	1.12	237	0.23	1.07	3.67	0.21	1.02	1.04	100
L29	0.37	1.42	6.64	0.64	1.08	1.04	94	0.31	1.23	4.76	0.62	1.03	1.25	299	0.34	1.34	5.67	0.61	1.01	0.94	156
L30	0.29	1.22	1.67	0.82	1.04	1.54	63	0.35	1.48	5.28	0.46	1.05	1.08	206	0.41	1.74	5.10	0.55	1.01	0.90	106
L31	0.28	1.39	7.43	0.35	1.01	1.02	77	0.18	0.89	8.44	0.30	1.50	1.17	244	0.28	1.37	6.47	0.25	1.00	0.94	115
L32	0.16	0.77	9.50	0.70	1.03	1.11	201	0.24	1.16	10.64	0.70	1.26	2.43	327	1.24	5.95	6.79	0.58	1.01	0.99	95
L33	0.29	1.51	5.90	0.87	1.01	0.99	126	0.26	1.36	3.77	0.88	1.08	1.33	368	0.26	1.32	4.10	0.86	1.00	0.91	139
L34	0.06	0.31	7.63	0.92	1.07	1.04	229	0.21	1.11	6.13	0.87	1.03	1.20	345	0.13	0.71	8.56	0.89	1.01	0.91	151
L35	0.26	1.26	4.24	0.70	0.95	0.87	69	0.28	1.36	3.31	0.78	1.02	1.11	272	0.30	1.47	2.89	0.70	1.00	0.90	174
L36	0.27	1.56	2.84	0.29	1.03	1.01	83	0.23	1.37	3.21	0.26	1.25	1.23	297	0.20	1.20	3.29	0.30	1.03	0.96	199
L37	0.17	0.71	6.34	0.53	1.01	0.98	82	0.19	0.84	5.21	0.50	1.02	1.06	249	0.18	0.80	7.52	0.34	1.01	0.98	72
L38	0.39	1.67	4.09	0.39	1.02	0.96	64	0.35	1.49	4.18	0.38	1.00	1.05	232	0.24	1.03	6.96	0.37	1.01	1.06	79
L39	0.36	1.62	3.16	0.27	1.00	1.01	96	0.33	1.47	3.77	0.32	1.10	1.56	311	0.30	1.32	3.25	0.31	1.01	0.90	132
L40	0.40	1.42	2.55	0.20	1.04	1.11	232	0.39	1.39	2.65	0.19	1.15	1.58	597	0.34	1.22	2.77	0.17	1.02	0.97	260
L41	0.51	2.26	5.63	0.53	0.97	0.95	81	0.33	1.47	7.59	0.56	1.03	1.33	255	0.30	1.33	8.73	0.50	0.99	0.91	108
L42	0.37	1.60	4.80	0.37	0.99	1.08	95	0.28	1.19	4.07	0.38	1.02	1.42	259	0.26	1.11	4.11	0.38	1.03	1.46	149
L43	0.37	1.61	6.28	0.28	1.00	0.92	89	0.32	1.40	4.73	0.29	1.03	1.25	246	0.32	1.42	6.48	0.29	1.03	0.90	137
L44	0.32	1.39	6.67	0.73	1.05	1.00	110	0.18	0.79	7.31	0.84	1.02	1.08	263	0.29	1.25	8.04	0.82	1.02	0.92	121
L45	0.44	1.50	2.93	0.47	1.03	1.04	143	0.39	1.31	3.06	0.40	1.06	1.45	349	0.4	1.53	3.08	0.45	1.00	1.00	195
L46	0.35	1.43	5.48	0.23	1.05	1.08	74	0.27	1.12	6.38	0.39	1.06	1.73	216	0.37	1.51	5.81	0.33	1.04	1.16	128
L47	0.31	1.27	8.90	0.67	1.13	1.46	357	0.33	1.33	9.29	0.63	1.19	1.85	694	0.29	1.19	9.37	0.72	1.04	1.07	282
L48	0.22	1.20	6.55	0.33	1.00	0.93	23	0.36	1.99	7.11	0.47	1.01	1.03	109	0.23	1.30	6.66	0.44	1.01	1.00	39
L49	0.29	1.60	5.37	0.54	0.99	1.00	56	0.14	0.78	6.90	0.41	1.04	1.29	198	0.22	1.23	3.24	0.51	1.03	0.93	107
L50	0.08	0.47	6.49	0.52	0.99	0.91	65	0.19	1.11	9.04	0.48	1.04	1.11	114	0.61	3.63	1.10	0.65	1.06	1.20	72
L51	0.06	0.35	5.39	0.64	1.09	1.17	265	0.13	0.74	9.21	0.89	1.04	1.09	272	0.26	1.51	7.55	0.86	1.02	1.00	89
L52	0.14	0.76	6.14	0.28	1.05	1.02	54	0.09	0.51	4.83	0.32	1.04	1.25	239	0.13	0.74	4.45	0.28	1.02	0.96	105
L53	0.34	1.35	6.48	0.34	1.00	0.99	74	0.34	1.38	6.36	0.31	1.05	1.34	282	0.44	1.76	3.91	0.29	1.00	0.98	207
L54	0.36	1.59	4.71	0.46	1.02	0.94	106	0.29	1.29	5.14	0.43	1.04	1.18	286	0.30	1.34	3.52	0.43	1.03	0.97	159
L55	0.81	4.84	9.20	0.76	0.99	1.01	24	0.18	1.06	9.19	0.61	1.01	1.17	114	0.11	0.69	8.62	0.59	1.00	1.01	50